Adaptive Wavelet-Based Turbulence Modeling for Compressible Flows in Complex Geometry

by

Eric Brown-Dymkoski

B.S., Washington State University, 2008

M.S., University of Colorado at Boulder, 2012

A thesis submitted to the

Faculty of the Graduate School of the

University of Colorado in partial fulfillment

of the requirements for the degree of

Doctor of Philosophy

Department of Mechanical Engineering

2016

This thesis entitled:
Adaptive Wavelet-Based Turbulence Modeling for Compressible Flows in Complex Geometry
written by Eric Brown-Dymkoski
has been approved for the Department of Mechanical Engineering

Oleg V. Vasilyev

Prof. Peter Hamlington

Prof. Daven Henze

Prof. Alireza Doostan

Prof. John A. Evans

Date

The final copy of this thesis has been examined by the signatories, and we find that both the content and the form meet acceptable presentation standards of scholarly work in the above mentioned discipline.

Brown-Dymkoski, Eric (Ph.D., Mechanical Engineering)

Adaptive Wavelet-Based Turbulence Modeling for Compressible Flows in Complex Geometry

Thesis directed by Prof. Oleg V. Vasilyev

Turbulent flows, noted for their chaotic dynamic and multiscale nature, are notoriously difficult and expensive to simulate accurately for problems of engineering interest. Adaptive wavelet-based methods have shown promise to this end with their ability to efficiently resolve local, coherent structures with *a priori* accuracy control. Here the methods are extended to the compressible regime, where thermodynamic and variable density effects interact with the turbulent flow.

The adaptive wavelet collocation method (AWCM) exploits spatio-temporal intermittency in turbulent flows through multiresolution analysis. The highest fidelity approaches, wavelet-based direct numeric simulation and coherent vortex simulation, capture all scales of the energy cascade. The so called stochastic-coherent adaptive large eddy simulation (SCALES) method, however, requires the implementation of a subgrid-scale (SGS) model. A compressible kinetic energy equation-based approach and a minimum dissipation model are adapted to the SCALES framework. For the k-equation model, nonlinear filtered terms are scaled by the SGS kinetic energy and model coefficients are locally determined through dynamic procedures. Stability of turbulent stress and heat flux is enhanced by the SGS kinetic energy field, allowing backscatter of modeled terms.

This work seeks to extend the capabilities of AWCM towards flow of engineering interest. In order to efficiently simulate bounded, complex geometry flows using a proposed hybrid adaptive-wavelet/curvilinear coordinate approach. The AWCM has a notable shortcoming in that mesh refinement is isotropic. A coordinate system transform can be used to stretch the grid and introduce local anisotropy, more effectively resolving arbitrarily oriented boundary layers while still preserving the rectilinear computational space necessary for the adaptive wavelet transform. A volume penalization method for compressible flows has been developed to introduce solid surfaces with arbitrary boundary conditions.

Dedication

For my Mother and my Father.

Acknowledgements

My advisor, Dr. Oleg V. Vasilyev, has been central in both my education and development as a scientist. He has provided endless guidance, challenge, and encouragement. Most of all, I would like to acknowledge the profound support and respect that he extends to his students.

I would like to thank my dissertation committee: Dr. Peter Hamlington, Dr. Daven Henze, Dr. Alireza Doostan and Dr. John A. Evans. I would also like to thank the members of my research group, whose contributions to my work are countless: Nurlybek Kasimov, Alireza Nejadmalayeri, Scott Reckinger, Shannon Reckinger, and Scott Wieland, along with all past members of the Multi-Scale Modeling and Simulation Lab which I will always be humbled to have been a part of.

Lastly, I would like to thank all of the friends and family, and teachers who have provided support, given encouragement, and taught me first. It takes a village.

Contents

Chapter

Tables

Table

Figures

Figure

Chapter 1

Introduction

1.1 Motivation and Objective

Of physical phenomena, few are as difficult to understand and, paradoxically, as pervasive as turbulence. It appears in our plumbing, around aircraft, within engines, the weather, and the interstellar medium that flows through the cosmos. In spite of its ubiquity, comprehensive understanding of turbulence remains elusive, as it is highly nonlinear, chaotic and dynamic, with whirls forming and breaking unpredictably. Compressible regimes further complicate flows with variable density and thermodynamic effects that couple with the underlying motion. Chaos should not be confused with randomness, however. Turbulence has inherent structure, containing tangles of coherent vortices ranging across all scales. The contradiction between its omnipresence and opacity has made understanding and predicting turbulence one of the most important problems presented to science and engineering.

Computational simulations have made vast progress towards this end. They are not confronted with the same instrumentation limits as with experiments, providing additional insight into flows. This is especially true for the compressible regime, which is often marked by high speeds and an experimentally unfavorable environment. However, accurate turbulent simulation has a very high computational cost due to wide ranges of spatial and temporal scales. In spite of rapidly developing computer hardware, modern capabilities are still extremely limited with respect to problems of engineering and scientific interest.

The computational difficulty arises from the fundamental multiscale nature of turbulence.

Energy input at the largest scales tends to chaotically transfer to progressively smaller scales, until the relative molecular viscous effects become significant and dissipate the motion into heat. This is the well known *turbulent energy cascade*. Andrey Nikolaevich Kolmogorov, the Soviet mathematician, deduced that the range of scales present scales with the Reynolds number as $\mathrm{Re}^{3/4}$ [38]. This implies that the degrees-of-freedom (DOF) for a discrete representation should scale as $O(\mathrm{Re}^{9/4})$ in three dimensions. For comparison, aircraft often operate at $\mathrm{Re} = O(10^7)$. Such simulations are far beyond even the most optimistic developments in computing power. The difficulties with simulating turbulence are compounded for applied flows of engineering interest. Complex flow geometries restrict the numerical methods that may be used and further constrain the computational landscape.

There are many different approaches to circumventing these problems. One notes that the Reynolds number scaling based upon Kolmogorov's work is a conservative estimate that assumes infinite homogeneity of information in space at the finest physical scales. Indeed, experimental and numerical investigations to-date show that turbulent fields are composed rather of a chaotic array of intermittent structures. Adaptive techniques can therefore be used to exploit this intermittency and reduce the total DOF by several orders of magnitude by accounting for localized variation in the flow. One such approach, the adaptive wavelet collocation method (AWCM), uses multiresolution analysis to refine the mesh on local structures and track them through time. Wavelet collocation is distinguished from other adaptive methods as it rigorously maintains consistent accuracy of the discrete solution *a priori*. As such, it optimizes the number of grid points by retaining only the "important" flow information, and either neglecting or modeling the unresolved signal. The corresponding high compression of this sparse data representation minimizes the memory footprint and reduces the computational costs of resolving the turbulent flow field.

A successful framework for adaptive wavelet-based turbulence modeling has previously been developed for incompressible flows. It provides continuously adjustable fidelity from well resolved direct numeric simulation (DNS) through very efficient large eddy simulation (LES) in a single, unified approach. Use of wavelet based methodologies are particularly well suited for aggressively

modeled turbulent flows [47]. The current work encompasses the extension of this framework to the compressible regime, where variable density and thermodynamic effects are of high interest and dramatically impact the flow field. This includes both bulk thermodynamic behavior, as well as compressible behavior of the turbulent motions themselves. In order to capture desired effects in the solution, AWCM must target prescribed accuracy toward appropriate fluid properties.

For flows of engineering interest, there is an additional need to account for complex geometry and arbitrary surfaces. Despite the advantages of AWCM for turbulent simulation, there are severe difficulties in applying the approach for complex and bounded configurations. The second generation wavelets popular for the solution of PDEs require a grid that is both topologically and geometrically rectilinear in order to leverage the fast ($O(\mathcal{N})$) adaptive transform algorithm[76]. This so-called "lifting scheme" is integral to the efficient grid refinement mechanism.

Additionally, AWCM is unable to distinguish anisotropy in solutions, implying a marked degradation of performance for bounded high-speed flows. Solid interfaces within the fluid introduce small scale boundary layers whose resolution is crucial for the accuracy. They inject turbulent energy via inherent instabilities. For separated boundary layers, the location of detachment and reattachment points dramatically impacts the flow field, including low order statistics.

Due to the extremely small thickness of the viscous sublayer, very high wall-normal resolution is required, even for modeled approaches, such as large eddy simulation (LES) and Reynolds averaged Navier-Stokes (RANS). At high Reynolds numbers, the computational cost associated with the boundary layer can form a large portion of the solution. The isotropic refinement mechanism of AWCM greatly compounds the cost, negating any advantage of the method. Isotropic adaptation cannot discriminate high correlations tangential to boundary layers from the steep gradients normal to the surface. This holds true for any sheet- and filament-like structures, resulting in gross over-resolution and prohibitively expensive sparse data representations of flow solutions.

Optimal approaches to capturing complex geometry in simulations must therefore address both the restriction imposed by the rectilinear topological requirement, as well as the inefficient isotropic resolution of surfaces. The current work is to develop an integrated computational envi-

ronment for the efficient simulation of compressible, turbulent flows in an arbitrary geometry using adaptive wavelet-based approaches.

1.2 Methodology

To exploit the spatio-temporal intermittancy of turbulent flows, AWCM utilizes multiresolution analysis to refine the grid upon coherent structures. A nonlinear wavelet filter discards localized modes associated with an insignificant contribution to the overall solution. The fidelity of the adaptive mesh representation to the underlying signal is controlled by a threshold parameter that can either be prescribed *a priori*, or determined through feedback functions during the course of the simulation. A principal advantage of AWCM is that the adaptive error is directly correlated to the local value of this filter threshold. Therefore, the discrete representation of specific variables and quantities of interest can be rigorously maintained at a prescribed accuracy.

Wavelet-based turbulence methods exploit the additional property of wavelet analysis to identify and filter structures based on the notion of coherency. In contrast, traditional large eddy simulation (LES) frameworks typically approach the modeling problem from the perspective of wavenumber. In that view, reduction of computational cost arises from assumption of some characteristic universality of turbulent structures below a certain length scale in the energy cascade. Wavelet approaches, however, propose that the stochastic and low energy coherent modes are most admissible for generalization.

A wavelet-based hierarchical framework for adjustable fidelity turbulence modeling has emerged from incompressible studies [30, 31, 47]. Simulations can be broadly categorized into three fidelity levels where specification of the wavelet filter threshold, $\varepsilon(\mathbf{x}, t)$, rigorously controls the filter and therefore the accuracy of the solution. Figure 1.1 outlines these classes, distinguished based on the wavelet coherency filtering, in contrast to traditional length scale modeling arguments.

Wavelet direct numerical simulation (WDNS) achieves the highest fidelity through the direct solution of the governing transport equations using a filtering threshold with a negligible error. This is a form of adaptive DNS where the spatial discretization accuracy is rigorously maintained.

In WDNS, reduced computational cost is only realized through the sparse data form of the solution fields. By comparison, traditional DNS would be represented by the nonadaptive grid that results from $\varepsilon = 0$ with the unclosed wavelet filtered terms vanishing.

Coherent vortex simulation (CVS) is a semi-deterministic approach that directly simulates the flow equations at a lower fidelity level by only resolving the coherent structures on the grid [23]. For strict CVS, it is assumed that the discarded modes form a purely stochastic signal at an ideal level, $\varepsilon_{\text{IDEAL}}$, as identified by a Gaussian distribution function in the subgrid scale (SGS) modes. The resolved signal, therefore, comprises of the de-noised coherent structures spanning all wavenumbers in the flow. In practical implementation, $\varepsilon_{\text{IDEAL}}$ is estimated [47, 58]. Though non-negligible, the residual terms can be truncated and an explicit closure model omitted while still maintaining a high degree of fidelity. Since dissipative length scales are explicitly resolved, kinetic energy is removed at the highest wavenumbers through molecular viscous terms. At these higher filtering levels, the sparse grid compression is substantially higher than WDNS, with improved cost scaling against Reynolds number for isotropic turbulence simulations [47]. While CVS was proposed based on the wavelet-filtered vorticity transport equations, similar behavior has been demonstrated for the filtered Navier-Stokes equations [30], permitting its use in a unified, adjustable fidelity modeling framework.

The highest compression ratios are achieved through so-called stochastic coherent adaptive large eddy simulation (SCALES) [30]. This approach combines tenets of CVS and LES by introducing SGS closure terms within the coherency filtering AWCM environment. With an aggressive ε, the lowest energy coherent motions are also discarded and their effect must therefore be modeled, including providing mechanisms for energy loss through unresolved viscous effects as the least energetic structures appear at the dissipative length scales in the turbulence cascade. In this manner, SCALES realizes a substantial reduction in the degrees of freedom compared to WDNS and CVS. Within traditional lowpass-filtered LES, it is assumed that the largest eddy structures are the most distinctive modes for a given flow regime, and the smallest have a universal character whose effects on the resolved field are sufficient to capture statistical behavior. The SCALES mothodology pro-

poses that it is the most energetic coherent modes that will dominate mixing, heat transfer, and other quantities of interest that are characteristic to specific flow configurations. The least energetic modes, therefore, are considered to be the most universal and permissive of subgrid modeling.

By using LES models with suitable properties, namely automatic shut-off for well resolved and laminar regions, these three approaches collapse into a single unified, hierarchical framework with continuously adjustable fidelity.

For compressible flows, WDNS and CVS approaches been previously studied [55, 58]. Implementation of SCALES has been limited to the incompressible regime. To formulate compressible, wavelet-based SCALES methodologies, corresponding SGS terms are used to close the wavelet filtered compressible Navier-Stokes equations. Naturally, this includes additional SGS modeling for the thermodynamic transport equation. As the adaptive refinement and *a priori* fidelity control of wavelet-based methods is particularly attractive for use in simulating complex flows, appropriate selection of LES closures need to reflect this environment. Many classic LES methods, especially variants on dynamic Smagorinsky and scaling models [28], rely on directional averaging for stabilization. Such a requirement can limit their applicability and fidelity for complex geometries.

Here, the implementation of several localized eddy viscosity models is proposed and studied. For incompressible SCALES, local dynamic kinetic energy models (LDKM) have been particularly successful due to their dynamic computation, stability, and localization properties, and a compressible analogue is examined. Additionally, low computational cost alternatives are proposed for targeting the approach toward applied engineering configurations.

In developing AWCM based methods for this problem space, it must be noted that the use of AWCM places several restrictions upon the discrete mesh. The nonlinear wavelet filter relies upon an efficient tensorial algorithm, limiting the solver to a rectilinear computational grid. While attractive for turbulence modeling, these limits have slowed the development of wavelet-collocation based approaches as a feasible industrial tool. On that topology, simulation of arbitrary complex geometries can be accomplished through the use of volume penalization methods, which are related to immersed boundary methods. The governing equations are modified, or penalized, to include

volumetric forcing terms within the space occupied by solid geometry. Specific boundary condition approximations arise from the nature and construct of these forcing terms.

Previous volume penalization approaches for the compressible regime have been limited in the type and nature of the boundary conditions that can be prescribed. A new method is presented that introduces hyperbolic forcing terms on the governing equations. This characteristic-based volume penalization (CBVP) method is fully generalized and allows formulation of penalization terms based on generic boundary conditions, including Dirichlet, Neumann and Robin.

Application of AWCM is further limited by the isotropic nature of the wavelet refinement mechanism, which is suboptimal for flow features with highly preferred refinement directions, such as boundary layers. A method for introducing local and spatially varying anisotropy is developed and introduced here. This adaptive-anisotropic wavelet collocation method (A-AWCM) uses coordinate transforms to permit arbitrary curvilinear meshes in physical space, while retaining the necessary computational environment for adaptive wavelet methods. The effect is to normalize highly anisotropic structures through the transform to computational space, on which AWCM grid refinement performs more efficiently. Many of the attractive properties of AWCM for simulation are retained in this integrated framework. The discretization error is still rigorously controlled, and a consistent accuracy of the physical space solution is maintained regardless of the geometry of the underlying (well conditioned) mesh. The generality of A-AWCM also permits the use of body-fitted meshing for many cases.

All of the simulations presented here utilize a fully parallel AWCM solver [49].

1.3 Organization

This dissertation is the conglomeration of three journal articles, organized as follows. Chapter 2 develops the Characteristic-Based Penalization Method [9]. It describes the general theory and specific application to solid obstacles within compressible viscous flows. This is part of a collaborative research effort with Nurlybek Kasimov, who developed the application for inviscid flows and generalized moving obstacles, presented elsewhere.

The adaptive-anisotropic wavelet collocation method framework is developed in Chapter 3 [8]. This is an approach for introducing complex geometry *meshes* into the AWCM framework, including the ability to anisotropically stretch local cells in order to more efficiently resolve sheet-like and filament-like features.

Finally, the extension of SCALES to compressible and wall bounded turbulent flows is presented in Chapter 4 [7]. Chapter 5 outlines general conclusions and topics of future research.

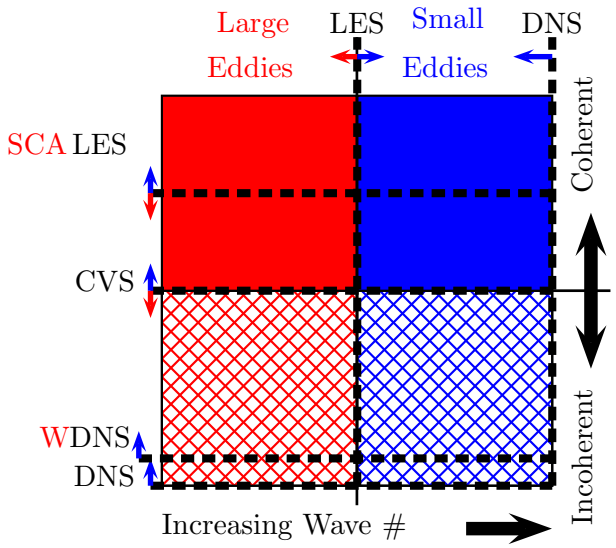

Figure 1.1: Coherency diagram of wavelet-based turbulence simulation methods compared with traditional lowpass filtered approaches. Turbulence modeling approaches can be considered either from the perspective of length scale or coherency. Wavelet threshold filtering discards the stochastic and lowest energy coherent modes. With an increasing ε, the approximation transitions through WDNS, CVS, and SCALES, in order of decreasing fidelity.

Chapter 2

A Characteristic Based Volume Penalization Method for General Evolution Problems Applied to Compressible Viscous Flows

2.1 Introduction

Numerical simulations of complex geometry flows in a computationally efficient manner, especially for moving surfaces, is a challenging problem. Solid bodies are introduced by imposing appropriate boundary conditions upon surfaces, and to that end, several approaches are used. These methods can be separated into two major groups: body-fitted mesh and immersed boundary methods. The former uses conformal grids with nodes coincident to the surface of an obstacle, while the latter employs forcing upon the constitutive equations to impose appropriate boundary conditions.

Though body-conformal meshes allow for exact boundary conditions (BC's) to be imposed, the grid must be carefully constructed to precisely fit an obstacle. In most cases, this precludes the use of structured Cartesian grids. The process of mesh generation is highly dependent upon the obstacle geometry, and can become computationally quite expensive, especially for complex surfaces. This issue is compounded for moving or deforming obstacles, which require continuous adaptation or re-meshing throughout computation of the solution [43].

Immersed boundary methods avoid the cost and complications of body meshing by introducing the effects of obstacles upon the governing equations themselves. Solid body effects, thus embedded within the flow itself, obviate the rigors of positioning nodes upon a surface. Immersed boundary forcing can be applied either to the continuous or discretized equations. While applying

discretized forcing allows for a high level of control based upon the numerical accuracy and conservative properties of the discretization method, this approach lacks generality and flexibility across solvers [43].

Volume penalization, on the other hand, imposes the effects of solid bodies by introducing forcing terms on the continuous equations and the resulting evolutionary equations are discretized and solved in the normal manner. One such method is the Brinkman Penalization Method (BPM) [1], which was originally developed for solid, isothermal obstacles in incompressible flows. A principal strength of Brinkman penalization is that error can be rigorously controlled *a priori*, with the solution converging to the exact in a predictable fashion [24, 35]. Much work has been done to refine BPM for various numerical techniques, including pseudospectral methods [35, 52, 32], wavelets [41, 71], and finite-element/finite-volume methods [54]. Of particular note is the impact of volume penalization upon pseudospectral methods, as it has allowed for arbitrary domain geometry and the ability to circumvent the limitations of periodic boundaries [52, 32]. In addition to being extended to various solvers, BPM has been expanded beyond the original application of incompressible flows to compressible [41, 5] and inviscid [2] regimes.

For all of this progress, boundary conditions imposed by BPM have lacked generality, especially for compressible flows. They have been typically limited to isothermal obstacles and slip/no-slip conditions for the inviscid and viscous regimes, respectively. Additional boundary conditions have been developed on an individual, and usually problem specific, basis. Though homogeneous Neumann condition was recently formulated for scalar mixing and advection-diffusion problems [33], general treatment of homogeneous/inhomogeneous Robin and Neumann conditions has been limited to finite-volume/finite-element methods [54]. In this way, BPM has been inapplicable for many fluid problems, notably those demanding heat-flux and insulating boundary conditions on solid surfaces.

In this work, we propose an extension of volume penalization that introduces characteristic-based forcing terms, exploiting their hyperbolicity to impose general homogeneous and inhomogeneous Neumann and Robin boundary conditions. This Characteristic-Based Volume Penalization

(CBVP) method is flexible and can be applied to parabolic and hyperbolic evolutionary equations; in this paper, CBVP is examined for both scalar diffusion and the fully compressible Navier-Stokes equations. As with BPM, this method maintains rigorous control of the error through *a priori* chosen parameters for all boundary conditions.

Characteristic-based volume penalization is well suited for use with adaptive mesh refinement (AMR). As volume penalization does not require body-conformal meshing, high resolution is required around surfaces for computational accuracy and proper definition of geometry. The use of AMR grids maintains solid geometry resolution without over-resolving flow structures. Additionally, the number of nonphysical points lying inside of the obstacle can be minimized to those necessary to support the boundary conditions, which is particularly important for obstacles inhabiting a large portion of the computational domain. All of the results reported in this paper were obtained using the Adaptive Wavelet Collocation Method (AWCM), a general numerical solver which utilizes a wavelet decomposition to dynamically adapt on steep gradients in the solution while retaining a predetermined order of accuracy [70, 73, 74]. Employing a rectilinear grid, AWCM precludes the use of body-fitted meshes to impose solid obstacles for all but the most simple geometries. Therefore, volume penalization is a natural means for introducing solid obstacles. As the geometry definitions are treated as any other flow variable by AWCM, and the local grid efficiently and dynamically adapts to resolve surfaces, even for moving obstacles.

2.2 Characteristic-Based Volume Penalization

2.2.1 Penalized Boundary Conditions

Characteristic-Base Volume Penalization imposes Dirichlet, Neumann, and Robin type boundary conditions by introducing forcing terms into the constitutive equations. Consider a domain Ω containing obstacles O_m, and governed by a generalized evolution equation

$$\frac{\partial u}{\partial t} = \text{RHS} \tag{2.1}$$

outside of O_m, where RHS is simply the physical right hand side forcing terms. Equation (2.1) can be hyperbolic or parabolic in nature. A masking function, $\chi(\mathbf{x}, t)$, is defined across Ω, where

$$\chi(\mathbf{x}, t) = \begin{cases} 1 & \text{if } x \in O_m, \\ 0 & \text{otherwise,} \end{cases}$$

separates the domain into a physical region and a penalized region defined by the solid obstacle.

Dirichlet conditions are imposed in the same fashion as with the Brinkman penalization method [41, 71]. For the boundary condition $u = u_0(\mathbf{x}, t)$ on an obstacle surface $\partial O_m(\mathbf{x}, t)$, the constitutive equation (2.1) is modified into the penalized equation

$$\frac{\partial u}{\partial t} = (1 - \chi) \times \text{RHS} - \frac{\chi}{\eta_b} \left(u - u_0(\mathbf{x}, t)\right) + \chi \nu_n \frac{\partial^2 u}{\partial x_i, \partial x_i}, \tag{2.2}$$

with summation implied over repeated indices. Convergence of the penalization parameter, as $\eta_b \to 0$, controls the error on the solution [1] by decreasing the timescale of the forcing term. Note that moving and deformable obstacles are defined in the penalized equation (2.2) by transient mask $\chi(\mathbf{x}, t)$ and boundary condition $u_0(\mathbf{x}, t)$ functions.

Typically, Brinkman penalization retains the constitutive equations inside of the obstacle and the penalization terms are simply appended where $\chi = 1$ [1]. The physical viscosity ensures smoothness and continuity of the solution. In departure from this convention, CBVP removes the physical terms, RHS, from within the obstacle in order to prevent secondary effects of coupled systems of equations from contaminating the desired boundary conditions. This allows for consistent control over the penalization scheme, regardless of the external physical terms.

In the formulation (2.2), removal of the constitutive equations from inside O_m necessitate the use of the penalized terms with nonphysical diffusion of strength ν_n in order to avoid creation of the discontinuous solution across the obstacle boundary. The use of numerical viscosity lends flexibility and generality to the method, as ν_n can be prescribed based on the particular numerical environment. Since continuous fluxes across the obstacle boundary are unnecessary, the diffusion term is not written in divergence form to enforce continuity through the first derivative. The use of a conservative viscous term across the discontinuous function $\chi\nu_n(x)$ would result in discontinuous

derivatives at the interface of the obstacle.

Since the nonphysical diffusion contributes to boundary condition error, the coefficient ν_n is prescribed to be the minimal necessary for the stability of the numerical method. The diffusive length scale, which must be sufficiently resolved, can be determined through order of magnitude analysis considering diffusive strength ν_n and a penalization timescale of η_b. For a resolution of Δx within O_m, the diffusive coefficient must be $\nu_n \geq O(\Delta x^2/\eta_b)$.

The Neumann condition, $\partial u/\partial \mathbf{n} = q(\mathbf{x}, t)$ for inward-oriented surface normal $\mathbf{n} = n_k$, is imposed by introducing forcing upon the derivatives of u. Since the volume of the obstacle is penalized rather than just the surface, the surface normal is defined everywhere by linear extension throughout O_m. This leads to the penalized, hyperbolic equation

$$\frac{\partial u}{\partial t} = (1-\chi) \times \text{RHS} - \frac{\chi}{\eta_c}\left(n_k \frac{\partial u}{\partial x_k} - q(\mathbf{x}, t)\right). \tag{2.3}$$

With the normal defined everywhere, (2.3) has inward-pointing characteristics that extend perpendicular to the surface into O_m. This propagates the solution from the surface inward with a spatial growth or decay, based on q, that enforces the desired derivative. The inward nature of the characteristics also prevents the nonphysical solution within O_m from propagating outwards, so that the external solution is only affected through the surface derivative imposed by penalization. Since the constitutive equations might also be hyperbolic, as in the case with compressible flows, removal of the physical right hand side terms from (2.3) ensures inward orientation of characteristics within the penalized region.

The Robin boundary condition, of the form $a(\mathbf{x}, t)u + b\partial u/\partial \mathbf{n} = g(\mathbf{x}, t)$ with $b > 0$, is similarly penalized through the hyperbolic equation

$$\frac{\partial u}{\partial t} = (1-\chi) \times \text{RHS} - \frac{\chi}{\eta_c}\left(a(\mathbf{x}, t)u + b n_k \frac{\partial u}{\partial x_k} - g\right). \tag{2.4}$$

Here, the hyperbolic propagation is accompanied by an additional source term, au, indicating that the penalized Neumann condition (2.3) is simply a special case of the Robin condition where $a = 0$. For penalization, it is important that the Robin boundary condition is expressed so that b

is positive, otherwise the characteristics within O_m will point outward. For simplicity, it is defined here as a constant.

It can easily be seen that at steady-state within O_m, both the Neumann- (2.3) and Robin-type (2.4) penalized equations converge to the desired boundary condition. Since the penalization timescale is controlled through the parameter η_c, selecting $\eta_c << 1$ causes (2.3) and (2.4) to become quasi-steady within O_m on the normalized problem timescale, therefore imposing the intended BC on the surface. As $\eta_c \to 0$, the increased disparity in timescales asymptotically controls the penalization error. However, reducing the error increases the computational complexity. Since $1/\eta_c$ is the characteristic velocity for (2.3-2.4), a reduction of η_c is also accompanied by increased stiffness, a well known problem with Brinkman penalization that is mitigated through stiffly-stable solvers [41].

2.2.2 Stability and Penalization of Closed Obstacles

In some cases, the hyperbolicity of penalized equations can lead to difficulties when (2.3) and (2.4) are applied across all of Ω. Since the characteristics all follow surface normals, a situation can arise for some geometry, including all closed obstacles, where characteristics converge and create inconsistencies and discontinuities. By defining the normal throughout the volume of O_m by the gradient of a scalar distance function,

$$\mathbf{n} = \nabla d, \tag{2.5}$$

where d is the the distance to the nearest point on a surface, it can be seen that characteristics of (2.3) and (2.4) will converge wherever d is nondifferentiable. This occurs wherever a point inside O_m is equidistant from multiple surfaces.

To circumvent this difficulty, local differential schemes can be implemented, if possible, and regions of intersecting characteristics omitted from the solution. For some solvers, such as AWCM which employs global derivatives, this is not possible or practical. In such a case, inconsistencies with characteristics are avoided by only applying the hyperbolic terms in a narrow region along the surface within O_m, as shown in Figure 2.1. This region is only wide enough to accommodate

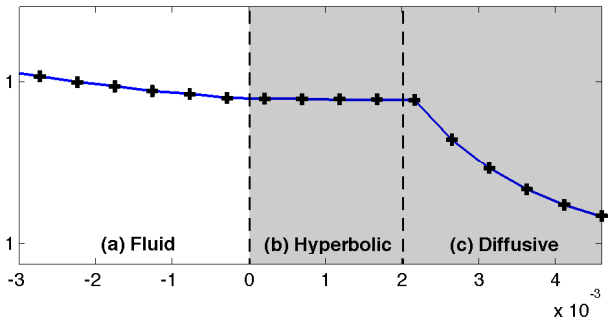

Figure 2.1: A dual-zone penalization approach for resolving intersecting characteristics. An obstacle consists of hyperbolic (b) and diffusive (c) regions. The hyperbolic zone contains the CBVP terms and provides boundary condition support for the solid-fluid interface. The diffusive zone provides continuity throughout Ω.

the differencing stencil for external points located immediately outside of the interface. Additional points within the obstacle are unnecessary to support external derivatives.

The interior region, where the hyperbolic penalization terms are not applied, is governed by weak diffusion to provide support for global derivatives. Unlike the diffusion used to stabilize the penalized Dirichlet condition (2.2), this diffusion is defined in conservative form, maintaining continuous fluxes throughout O_m.

Transition between the hyperbolic and the diffusive regions often introduces a discontinuous derivative. To avoid forming oscillations, the differencing stencil for hyperbolic terms must be prevented from crossing the transition and any potential discontinuities. Points near the transition employ upwind-biased differencing with fully upwind schemes immediately adjacent to the transition. Experience has shown that oscillations arising from ill-constructed zone transitions and exacerbated by penalization stiffness can propagate outward and degrade the physical solution in spite of the inward-pointing characteristics. The hyberbolicity does, however, prevent the solution in the diffusive region from affecting the solution on the obstacle surface. Using low-order, upwind-biased differencing and a narrow convective zone has the added benefit of increased stability with implicit methods, allowing calculations on the external, physical timescale.

These additional considerations of a dual zone approach emphasize the need to remove the

physical terms within O_m from the penalized equations (2.2-2.4) to ensure that all characteristics point inward on the obstacle, regardless of the constitutive equations. Furthermore, retention of physical coupling within O_m could lead to steep gradients and other spurious structures contaminating other boundary conditions. Obstacles that employ both characteristic-based and Dirichlet-type penalization on separate variables are particularly susceptible to adverse coupling effects if physical terms are not removed.

2.3 Penalization of the Navier-Stokes Equations

A principle strength of this method is the ability to easily prescribe boundary conditions in a systematic manner. Intentionally general, CBVP can be used for a variety of physical systems and evolution equations, including fluid regimes. Here penalization is applied for compressible, viscous flows around complex geometries.

2.3.1 Governing Equations

The fluid is governed by the fully compressible Navier-Stokes equations. The nondimensionalized continuity, momentum and energy equations in conservative form are

$$\frac{\partial \rho}{\partial t} = -\frac{\partial \rho u_j}{\partial x_j}, \tag{2.6}$$

$$\frac{\partial \rho u_i}{\partial t} = -\frac{\partial (\rho u_i u_j)}{\partial x_j} - \frac{\partial p}{\partial x_i} + \frac{1}{Re_a}\frac{\partial \tau_{ij}}{\partial x_j}, \tag{2.7}$$

$$\frac{\partial \rho e}{\partial t} = -\frac{\partial}{\partial x_j}\left[(\rho e + p)\, u_j\right] + \frac{1}{Re_a}\frac{\partial (u_i \tau_{ij})}{\partial x_j} + \frac{1}{(\gamma - 1)}\frac{1}{Re_a Pr}\frac{\partial}{\partial x_j}\left(\mu \frac{\partial T}{\partial x_j}\right), \tag{2.8}$$

where

$$p = \frac{\rho T}{\gamma}, \tag{2.9}$$

$$\tau_{ij} = \mu\left(\frac{\partial u_i}{\partial x_j} + \frac{\partial u_j}{\partial x_i} - \frac{2}{3}\frac{\partial u_k}{\partial x_k}\delta_{ij}\right), \tag{2.10}$$

$$\mu = \frac{1 + S_1}{T + S_1}(T)^{3/2}, \tag{2.11}$$

$$e = \frac{1}{2}u_i u_i + c_p T - \frac{p}{\rho}, \tag{2.12}$$

Re_a is the acoustic Reynolds number and Pr is the Prandtl number. Length scales are based on the characteristic length of the obstacle, L. The velocity $\mathbf{u}$ is nondimensionalized based on the reference speed of sound c_0, time based on L/c_0, specific energy on c_0^2, density on ρ_0, pressure on $\rho_0 c_0^2$, viscosity on μ_0, thermal conductivity on $\mu_0 c_{p_0}$, and temperature on T_0. Here, Sutherland's law is used for temperature-dependent viscosity, and the constant S_1 is normalized to the reference temperature.

For the benchmark problems considered in this paper, no-slip and adiabatic/heat flux conditions are imposed on velocity and temperature. These boundary conditions, and their corresponding penalization, are

$$u_i|_{\partial O_m} = u_{0i}, \qquad \frac{\partial u_i}{\partial t} = (1-\chi) \times \text{RHS} - \frac{\chi}{\eta_b}\left(u_i - u_{0i}\right) + \chi \nu_n \frac{\partial^2 u_i}{\partial x_j \partial x_j}, \tag{2.13}$$

$$n_k \frac{\partial T}{\partial x_k}\bigg|_{\partial O_m} = q, \qquad \frac{\partial T}{\partial t} = (1-\chi) \times \text{RHS} - \frac{\chi}{\eta_c}\left(n_k \frac{\partial T}{\partial x_k} - q\right), \tag{2.14}$$

where $u_{oi} = u_{oi}(\mathbf{x}, t)$ and $q = q(\mathbf{x}, t)$ for the generalized case of moving or deforming obstacles and inhomogeneous heat flux.

In order to apply these penalized boundary conditions to the constitutive equations (2.6-2.8), the equations of state (2.9 -2.12) are used to determine consistent penalization of the integrated variables ρ, ρu, and ρe, from the native variables u and T. However, without appropriate penalized equation for ρ, the equations of state are under-constrained. Additionally, a penalized equation for density must be provided within O_m since ρ is solved across all of Ω. For exact boundary conditions, the Navier-Stokes equations are well posed through no-slip and heat-flux conditions, so the continuity equation is solved for density. The simplest approach, then, is to analogously retain the continuity equation inside of a penalized obstacle, however this was found by Liu and Vasilyev [41] to cause unacceptable errors. Therefore, the difficulty is to determine an additional penalized equation for ρ that accurately matches the problem physics at the interface without imposing additional constraints upon the flow.

There are two main approaches to evolutionary penalization, each with their own advantages. Physical models can be used within the penalized region to mimic the solution on the interface, or an

evolutionary condition imposed that passively provides continuity and smoothness. Characteristic-based passive evolutionary conditions have the advantage of generality, though implementation involves time integration of an additional equation.

The passive evolutionary condition is built upon the CBVP Neumann condition (2.3). Due to the inward pointing characteristic, the solution on the interface is determined by fluid physics with the derivative imposed by the penalized volume of O_m. By using an inhomogeneous Neumann condition on ρ where the target derivative throughout O_m is the normal derivative on the surface, density becomes completely passive to the fluid physics. This is done by introducing an additional equation and taking advantage of the hyperbolicity of CBVP to extrapolate the density derivative from the solid-fluid interface into O_m along the surface normal by

$$\frac{\partial \Phi}{\partial t} = -\frac{\chi}{\eta_c} n_k \frac{\partial \Phi}{\partial x_k}, \tag{2.15}$$

where

$$\Phi = (1-\chi)\, n_k \frac{\partial \rho}{\partial x_k} + \chi \Phi. \tag{2.16}$$

Defining Φ across all of Ω provides the necessary boundary condition from ρ for the hyperbolic equation (2.15), which is solved only within O_m. In this way, density derivatives are physically determined outside of the obstacle via the continuity equation and extrapolated inside O_m by integrating (2.15). Therefore, Φ is fully passive to the physical solution.

Within the penalized region, Φ becomes the target for the inhomogeneous Neumann condition on ρ, yielding the evolutionary condition

$$\frac{\partial \rho}{\partial t} = (1-\chi) \times \mathrm{RHS} - \frac{\chi}{\eta_c}\left(n_k \frac{\partial \rho}{\partial x_k} - \Phi \right). \tag{2.17}$$

Since both the solution ρ and its first derivative are propagated along the inward characteristic, both are determined by the fluid physics. The flux, however, is discontinuous across the solid-fluid interface.

Consistent penalization of the integrated compressible variables ρu_i and ρe is easily deter-

mined from physical boundary conditions and the equations of state (2.9-2.12) by noting that

$$\frac{\partial \rho u_i}{\partial t} = u_i \frac{\partial \rho}{\partial t} + \rho \frac{\partial u_i}{\partial t}, \tag{2.18}$$

$$\frac{\partial \rho e}{\partial t} = e \frac{\partial \rho}{\partial t} + \rho u_i \frac{\partial u_i}{\partial t} + c_v \rho \frac{\partial T}{\partial t}. \tag{2.19}$$

The temporal derivatives of u_i, T, and ρ in (2.18) and (2.19) are defined by the penalized native variables (2.13-2.14) and (2.17). Upon substitution and writing the equations in terms of integrated variables, the penalized equations become

$$\frac{\partial \rho}{\partial t} = (1-\chi) \times \text{RHS} - \frac{\chi}{\eta_c} \left(n_k \frac{\partial \rho}{\partial x_k} - \Phi \right) \tag{2.20}$$

$$\frac{\partial \rho u_i}{\partial t} = (1-\chi) \times \text{RHS} - \chi \left[\frac{1}{\eta_b} \rho \left(u_i - u_{0i} \right) + \rho \nu_n \frac{\partial^2 u_i}{\partial x_j \partial x_j} + \frac{1}{\eta_c} u_i \left(n_k \frac{\partial \rho}{\partial x_k} - \Phi \right) \right] \tag{2.21}$$

$$\frac{\partial \rho e}{\partial t} = (1-\chi) \times \text{RHS} - \chi \left[\frac{1}{\eta_c} \left(n_k \frac{\partial \rho e}{\partial x_k} \right) + \frac{\rho (u_j - u_{0j}) u_j}{\eta_b} - \frac{\rho u_j}{\eta_c} n_k \frac{\partial u_j}{\partial x_k} - \rho u_j \nu_n \frac{\partial^2 u_j}{\partial x_i \partial x_i} - \frac{1}{\eta_c} e \Phi - \frac{1}{\eta_c} c_v \rho q \right], \tag{2.22}$$

where the the physical RHS terms in (2.20 - 2.22) are the Navier-Stokes equations (2.6 - 2.8).

An alternative method of treating ρ within the penalized region is by actively matching the physics of the fluid. This eliminates the need for additional integrated equations. From the momentum equation (2.7), assuming that the error on the no-slip condition is sufficiently small, the derivative of the full normal stress at a solid surface is zero. Since volume penalization acts across all of O_m and not just on the surface, it is inappropriate to directly apply the Neumann condition on the normal stress as a third BC, as a spurious stress in the penalized region is required to ensure smoothness of the velocity solution across the interface. However, for flow regimes with a sufficiently small gradient in the normal shear stress, that is

$$O \left(\frac{1}{Re_a} \frac{\partial n_k \tau_{nn}}{\partial x_k} \right) << 1, \tag{2.23}$$

through order of magnitude analysis, the normal stress derivative can be approximated as

$$\left. \frac{\partial n_k \sigma_{nn}}{\partial x_k} \right|_{O_m} \approx n_k \left. \frac{\partial p}{\partial x_k} \right|_{O_m} \approx 0. \tag{2.24}$$

Attached boundary layer flows and linear acoustic regimes, among others, typically satisfy this criterion. A consistent boundary treatment for density can therefore be determined from (2.24), the equation of state (2.9), and the condition on temperature (2.14). As this condition attempts to match the fluid physics, violation of aforementioned assumptions leads to large errors and oscillations which are particularly problematic for adaptive grids.

For some of the problems presented in this paper, low viscosity and a stationary, adiabatic obstacle makes the problem well suited for imposing this normal stress approximation (2.24). Noting that the no-slip condition for a stationary obstacle can be expressed as $(\rho u)_{0i} = u_{0i} = 0$, the momentum equation can be directly penalized instead of velocity (2.13). By applying (2.24) as a third condition, the penalized Navier-Stokes equations are determined from (2.18) and (2.19) as

$$\frac{\partial \rho}{\partial t} = (1-\chi) \times \text{RHS} - \frac{\chi}{\eta_c}\left(n_k \frac{\partial \rho}{\partial x_k}\right) \tag{2.25}$$

$$\frac{\partial \rho u_i}{\partial t} = (1-\chi) \times \text{RHS} - \chi\left[\frac{1}{\eta_b}\rho u_i - \nu_n \frac{\partial^2 \rho u_i}{\partial x_j \partial x_j}\right] \tag{2.26}$$

$$\frac{\partial \rho e}{\partial t} = (1-\chi) \times \text{RHS} - \chi\left[\frac{1}{\eta_c}\left(n_k \frac{\partial \rho e}{\partial x_k}\right) + \frac{\rho u_j u_j}{\eta_b} - \frac{u_j}{\eta_c} n_k \frac{\partial \rho u_j}{\partial x_k} - u_i \nu_n \frac{\partial^2 \rho u_i}{\partial x_j \partial x_j}\right]. \tag{2.27}$$

This penalized system is more simple than (2.20-2.22), and does not require any additional integrated equations to calculate an evolutionary target ϕ. However, it is a form specific to a non-movable, non-deformable, adiabatic obstacle.

2.3.2 Error Estimation From Linear Asymptotic Analysis

While it is difficult to analyze convergence of the penalized Navier-Stokes equations directly, rigorous asymptotic analysis gives insight into the error of the penalization parameters η_b and η_c. Consider one-dimensional flow with an acoustic pulse reflecting off an obstacle. Error arising from the penalization can be examined in the fully reflected pulse.

For the entire domain, the amplitudes of the nondimensionalized flow variables are asymptotically expanded. The leading order expansions are identical in both cases where $\eta_b << \eta_c$ and $\eta_b >> \eta_c$, so $\eta = \max(\eta_b, \eta_c) << 1$ to preserve generality. The leading perturbation terms for both

the fluid and penalized regions are

$$\rho_f(x,t) = 1 + \epsilon\rho'_{0f} + \epsilon\eta\rho'_{1f} + \ldots, \qquad u_f(x,t) = \epsilon u'_{0f} + \epsilon\eta u'_{1f} + \ldots,$$
$$p_f(x,t) = \frac{1}{\gamma} + \epsilon p'_{0f} + \epsilon\eta p'_{1f} + \ldots, \qquad T_f(x,t) = 1 + \epsilon T'_{0f} + \epsilon\eta T'_{1f} + \ldots \tag{2.28}$$

For the fluid region, where $\chi = 0$, substitution into (2.25-2.27) and retaining only first order terms, in essence linearizing the equations, yields the system

$$\frac{\partial u'_f}{\partial t} + \frac{\partial p'_f}{\partial x} = 0, \tag{2.29}$$
$$\frac{\partial p'_f}{\partial t} + \frac{\partial u'_f}{\partial x} = 0, \tag{2.30}$$

for both zero- and first-order perturbation quantities. Viscous terms are neglected in the high Reynolds number limit, where $1/Re_a << \eta$. Additionally, the relation $\rho'_f = p'_f$ holds, and the flow is isentropic. The resulting system (2.29-2.30) is simply the linear acoustic equations, describing small amplitude pulses propagating through the fluid.

For the penalized region, where $\chi = 1$, substitution of the asymptotically expanded variables into (2.25-2.27) and retaining first order perturbation quantities yields

$$\frac{\partial \rho'_p}{\partial t} + \frac{1}{\eta_c}\frac{\partial \rho'_p}{\partial n} = 0, \tag{2.31}$$
$$\frac{\partial u'_p}{\partial t} + \frac{1}{\eta_b}u'_p - \nu_n\frac{\partial^2 u}{\partial x^2} = 0, \tag{2.32}$$
$$\frac{\partial p'_p}{\partial t} + \frac{1}{\eta_c}\frac{\partial p'_p}{\partial n} = 0. \tag{2.33}$$

Again, the isentropic relation $\rho'_f = p'_f$ holds.

The perturbation equations (2.31-2.33) form a linear hyperbolic system of PDEs with a single characteristic pointing inward on the penalized domain. Strong damping on velocity drives the solution towards the no-slip condition on timescale η_b, while strong convection on timescale η_c enforces the desired Neumann conditions. This implies $\eta_b < \eta_c$ to avoid excessive phase lag in reflected pulses as energy and mass are convected too quickly past the interface.

In order to examine the error convergence as $\eta_b, \eta_c \to 0$, the two systems (2.29-2.30) and (2.31-2.33) are solved on a one-dimensional split domain. Fluid occupies the semi-infinite region

$x < 0$ while $x \geq 0$ is penalized, placing the solid interface at the origin.

The D'Alembert solution in the fluid region, in terms of initial $(u_0'(x), p_0'(x))$ conditions and boundary values $(u_1'(t), p_1'(t))$ at the fluid-obstacle interface, is

$$u_f'(x,t) = \frac{1}{2}u_0'(x-t) + \frac{1}{2}p_0'(x-t) + \frac{1}{2}u_1'(x+t) - \frac{1}{2}p_1'(x+t) \tag{2.34}$$

$$p_f'(x,t) = \frac{1}{2}u_0'(x-t) + \frac{1}{2}p_0'(x-t) - \frac{1}{2}u_1'(x+t) + \frac{1}{2}p_1'(x+t) \tag{2.35}$$

for both zero- and first-order perturbations.

The solution in the penalized region can be determined for each variable independently. The first order perturbation of pressure is easily solved based on the propagation of the solution on the interface p_1' for a single characteristic with speed $\lambda = \frac{1}{\eta_c}$,

$$p_p'(x,t) = p_1'(t - \eta_c x). \tag{2.36}$$

The first order velocity perturbation of u_p' can be solved by transforming (2.32) into the form of an inhomogeneous heat equation through

$$w'(x,t) = e^{-\frac{t}{\eta_b}}(u'(x,t) - u'(0,t)). \tag{2.37}$$

Assuming continuity with the fluid domain through the first derivative, the solution of $w'(x,t)$ on the semi-infinite domain is known [11]. Provided that the limits of the solution are finite and constant as $x \to 0$ for parameter η_b, then the solution at the interface is $O(\eta_b)$, and normalized to $u^*(t) = (\nu_n \eta_b)^{-1}\, u_p'\big|_{x=0}$. Now considering the acoustic timescale $1 >> \eta_b$, the quasi-steady state solution to the boundary value problem (2.32) is found to be

$$u_p'(x,t) = \eta_b u^*(t) \exp\left(\frac{x}{\sqrt{\eta_b \nu_n}}\right). \tag{2.38}$$

Enforcing continuity and smoothness between the fluid domain (2.30,2.29) and penalized domain solutions (2.36,2.38) yields the acoustic solution with leading error terms

$$E = -\frac{1}{1-2\eta_c}\left[\eta_c\left(u_0'(-x-t) + p_0'(-x-t)\right) + \frac{\sqrt{\nu_n \eta_b}}{2}\int_0^{x+t} u^*(\xi)d\xi + \cdots\right], \tag{2.39}$$

on the reflected pulse for both p'_f and u'_f. The error due to the penalized Neumann condition on p is in phase with the reflected pulse, while both phase and amplitude error are introduced through the no-slip condition. The total error on $O(\eta_c, \eta_b^{1/2})$ reinforces that, optimally, the penalization parameters should be chosen so that $\eta_b < \eta_c$.

2.4 Numerical Results

An initial examination into the accuracy of each CBVP boundary condition is obtained through numerical simulation of the one-dimensional diffusion equation. Each boundary condition type can be applied individually and in a physically meaningful way. The fluid benchmark problems here encompass a representative set of various flow regimes. One-dimensional acoustic reflection provides error convergence that corresponds to the analytic asymptotic analysis. Penalization is also applied for a multidimensional closed obstacle with flow past a cylinder. A low-compressibility, steady state benchmark is given, as well as compressible vortex shedding to demonstrate unsteady flow regimes. Both homogeneous and inhomogeneous Neumann conditions are implemented.

2.4.1 Benchmark I: One-Dimensional Diffusion

Consider transient one-dimensional diffusion across a domain, $\Omega = [-0.25, 0.015625)$, with the penalized obstacle at $O = [0, 0.015625]$. The parabolic equation

$$\frac{\partial u}{\partial t} = k\frac{\partial^2 u}{\partial x^2}, \tag{2.40}$$

is penalized by

$$\frac{\partial u}{\partial t} = (1-\chi)\,k\frac{\partial^2 u}{\partial x^2} - \frac{\chi}{\eta_b}(u - U_0) + \chi\nu_n\frac{\partial^2 u}{\partial x^2}, \tag{2.41}$$

$$\frac{\partial u}{\partial t} = (1-\chi)\,k\frac{\partial^2 u}{\partial x^2} - \frac{\chi}{\eta_c}\left(\frac{\partial u}{\partial n} - q\right), \tag{2.42}$$

$$\frac{\partial u}{\partial t} = (1-\chi)\,k\frac{\partial^2 u}{\partial x^2} - \frac{\chi}{\eta_c}\left(au + b\frac{\partial u}{\partial n} - g\right) \tag{2.43}$$

for Dirichlet, Neumann, and Robin conditions, respectively. The penalized diffusion equation for the Dirichlet condition (2.41) has been solved analytically by Kevlahan and Ghidaglia [35], though

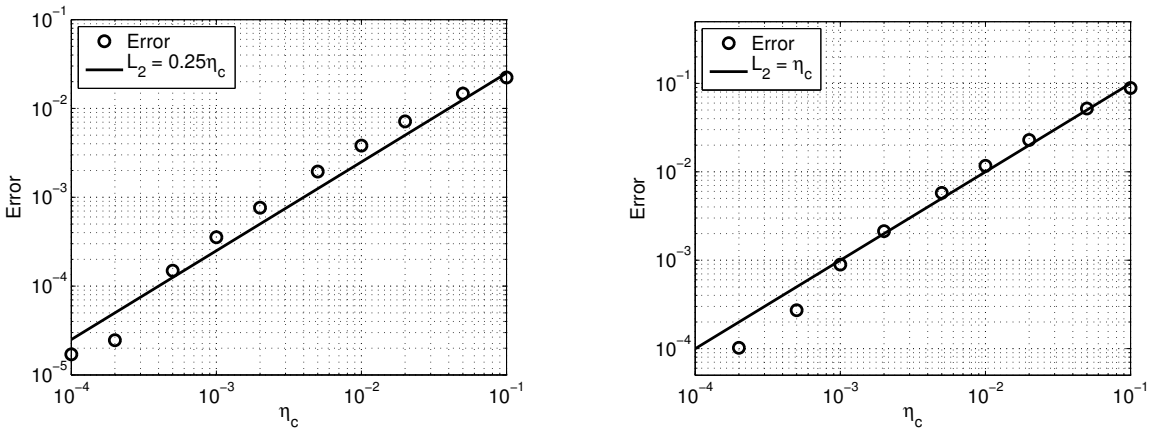

(a) Neumann (b) Robin

Figure 2.2: Time-averaged L_2-norm error for converging η_c for Neumann (2.2a) and Robin (2.2b) conditions for 1D diffusion.

in the context of Stokes flow, so here we only consider the characteristic-based penalization BC's, (2.42) and (2.43). At the solid boundary, the conditions $\partial u/\partial x = 0$ and $u + 2\partial u/\partial x = 5$ are applied for the Neumann and Robin cases, respectively. At $t = 0$, an impulsive step function of height $\delta u = 1$ is applied at $x = 0$ and allowed to diffuse across the domain. The error is determined while the solution at the interface, $u\,(x = 0)$, is still transient.

This problem uses a nonadaptive grid of either $M = 1089$ points. In determining the error, the solution is compared with numerical results with the exact boundary condition imposed and while the solution is still transient. The diffusive coefficient k were 0.5 and 1.0 for the Neumann- and Robin-type penalization respectively.

For comparison, the penalization for the Dirichlet condition converges as $O(\eta_b^{1/2})$ [35]. The error from penalization for both the Neumann and Robin conditions, in Figure (2.2) converges as $O(\eta_c)$. This is expected, as the Neumann condition is simply a special case of the Robin, where $a = 0$, and the convective behavior of both penalized equations is a fundamental departure from Brinkman penalization of the Dirichlet condition. The parameter η_c is not representative of a modeled porosity or impedance, but simply a disparate timescale for the relaxation of the internal zone. The lower convergence rate for the Dirichlet condition is a consequence of the penalization

terms forming a boundary layer inside of the obstacle in the immediate vicinity of the boundary.

2.4.2 Benchmark II: One-Dimensional Acoustic Reflection

To examine the error convergence for the Navier-Stokes equations, where two penalization types are imposed on coupled equations, consider one-dimensional acoustic reflection. Isentropic, low amplitude pulses bounce off of a solid obstacle, and the mass and energy losses from penalization observed in the reflected pulse. The penalized equations are solved on a domain $\Omega = [-0.65, 0.25]$, where the fluid occupies $\Omega_f = [-0.65, 0)$, and the solid obstacle is $O = [0, 0.25]$. The initial conditions consist of a localized pulse

$$\rho' = \rho u' = p' = 10^{-3} \left(\frac{x + 0.25}{0.2} - 1 \right)^4 \left(\frac{x + 0.25}{0.2} + 1 \right)^4, \tag{2.44}$$

$$-0.45 < x < -0.05. \tag{2.45}$$

The high order polynomial ensures that the piecewise function is continuous through the second derivative, avoiding discontinuous fluxes. This problem is solved in the inviscid limit, $Re_a = 10^8$, and at a very fine resolution with $M = [235930]$ points at the highest adaptive level. To observe proper error convergence, the Brinkman diffusion term, ν_n, is held constant at $\nu_n = 20\Delta x$, which allows for convergence of η_b across several orders of magnitude on this grid.

No-slip and adiabatic conditions are penalized at the solid interface. Since the viscosity is negligible for this problem, the approximation $\partial P/\partial x = 0$ provides the evolution condition for density at the interface, and the simplified form of penalized equations, (2.27-2.25), are used.

Figure 2.3 shows the error convergence on a fully reflected pulse for $\eta_b = [10^{-5}, 10^{-2}]$ where η_c is held constant at $\eta_c = 10^{-2}$ and 10^{-3}. The error convergence of both cases is the same, namely $O(\eta_b^{1/2})$, and neither case manifests significant errors from the characteristic-based terms. With the low amplitude, isentropic pulses and the inviscid limit, the asymptotic acoustic problem solved previously is well modeled here. The solution (2.39) indicates an in-phase error that is highly localized with a magnitude based on the initial pulse. At the pulse peak, the predicted error is $O(\eta_c)$ and rapidly diminishes with the local waveform amplitude. Therefore, the L_2-norm error of

the numerical solution is dominated by the phase lag consequential of the no-slip condition, even at $\eta_b = 10^{-5}$. This result demonstrates that reasonable error convergence can be achieved through only moderate values of η_c. This is beneficial as it mitigates the computational costs associated with the stiffness of the hyperbolic penalization terms.

An alternative to a constant ν_n is to set the coefficient based on the penalization timescale and resolution to ensure that diffusive effects are properly resolved. For α grid points in the diffusive length scale,

$$\nu_n = \frac{\alpha^2 \Delta x^2}{\eta_b}. \tag{2.46}$$

Experience has shown that $\alpha \approx 3$ points is the minimum required to avoid adaptive mesh-saturating oscillations using AWCM. With η_c and Δx remaining constant, the error on a fully reflected pulse does not converge with η_b, as shown in Figure 2.4. A reduction in η_b is met with a proportional increase in ν_n, resulting in an error that is insensitive to the penalization parameter. Rather, the error converges as $O(\Delta x)$. This agrees well with the result of the asymptotic analysis (2.39), which predicts an error of $O(\eta_b^{1/2} \nu_n^{1/2})$. By defining ν_n as in (2.46), the predicted error is $O(\alpha \Delta x)$. Since α is based on the tolerance of the solver for under-resolved features, this approach effectively minimizes the error while robustly preserving stability. The assumption still holds that η_b is much smaller than the normalized timescale of the fluid, however further reduction becomes superfluous and the error is set by the resolution of the grid near the interface.

2.4.3 Benchmark III: Low Mach Number External Flow

To extend CBVP to multiple dimensions, incompressible flow past a circular cylinder is considered. For steady flow, with $Re \leq 40$, the boundary layer behavior in the wake of a circular cylinder is well documented for both experimental and numerical cases [14, 69, 40, 20, 25, 19]. Since the streamlines are curved at the interface, the freestream Reynolds number is low, and the boundary layer separates from the trailing edge, the approximation $\partial P / \partial \mathbf{n} \approx 0$ breaks down and the simplified penalization (2.25-2.27) is no longer valid. Instead, the more robust form of the penalized Navier-Stokes equations, (2.20-2.22), using a characteristic-based evolutionary condition

on ρ. For accurate simulation of boundary layer separation, the proper treatment of the pressure gradient at the surface is important.

The flow is modeled as weakly compressible with $Ma = 0.03$ and freestream Reynolds number of $Re = 40$. A cylinder with radius $r = 0.5$ ($D = 1.0$) is centered on the origin of domain $\Omega = [-5, 10] \times [-5, 5]$, and the penalization parameters are $\eta_b = 5 \times 10^{-3}$ and $\eta_c = 10^{-2}$. The numerical viscosity is set according to (2.46), so that penalization error is automatically minimized based upon the highest resolution of the adaptive grid. Several different resolutions are used to demonstrate the control of the error through ν_n. Four cases are considered, where the maximum level of resolution on the adaptive grid is $\Delta x = 1/256, 1/512, 1/1024,$ and $1/2048$. The boundary layer separation point, θ, and the separated wake length L are both measured from the trailing edge of the cylinder.

Flow field velocity at steady state is shown in Figure 2.5. The results for each level of resolution are summarized in Table 2.1 and compared with previous numerical and experimental results. For increasingly refined grids, the solution converges to previously established values [14, 69, 40, 20, 25, 19]. The error arising from the no-slip condition manifests as a nonzero velocity on the surface, delaying boundary layer separation and decreasing the drag on the surface. By increasing the resolution, the viscous lengthscale decreases and with it the slip error at the surface. The large nu_n dependency and the high accuracy for moderate η_c reinforces that the error on the penalized Dirichlet condition remains the limiting factor.

2.4.4 Benchmark IV: Laminar Vortex Shedding

To verify the efficacy of CBVP for unsteady solutions, CBVP is applied for low Reynolds number vortex shedding around a two-dimensional cylinder. For $Ma = 0.20$ and $Re = 1000$, the flow past a cylinder remains laminar but experiences vortex shedding from the trailing edge. The domain discretization and penalization parameters remain as for the pseudo-incompressible case, namely $\Omega = [-5, 10] \times [-5, 5]$, $\eta_b = 5 \times 10^{-3}$ and $\eta_c = 10^{-2}$. Density is penalized with the evolutionary condition (2.17), and two temperature conditions are considered: an adiabatic

cylinder and constant heat flux at $\partial T/\partial \mathbf{n} = 1.5$.

The velocity and vorticity fields around an adiabatic cylinder are shown in Figure 2.6, as well as the temperature for both the adiabatic and heated cylinders. Periodic vortex shedding can be seen in the laminar wake behind the cylinder

In the case of the heated cylinder, the constant flux causes a temperature rise $O(0.1)$ along the surface. While Wang et al. [79] predict a decrease in the shedding frequency for a heated cylinder at low Reynolds number, the Strouhal number here is essentially unchanged by the increased temperatures. For laminar flows in the region of $Re \approx 1000$, the frequency is insensitive to the Reynolds number [6]. The increase in temperature, and corresponding increase in viscosity, is therefore insufficient to decrease the local Reynolds number enough to affect the periodicity of the wake. The heating is then best seen only through the direct effect on the temperature of the fluid. Examination of the temperature profile along an arbitrary surface normal, shown in Figure (2.7), verifies that the desired heat-flux of $q = 1.5$ is properly enforced on the penalized boundary.

Time variant lift and drag coefficients C_L and C_D, shown in Figure (2.8), and agree well with previous numerical results [6], though a slightly shorter shedding period can be seen. This higher frequency is reflected in a Strouhal number of $St = 0.245$, compared to $St = 0.238$ determined by Brentner et al. [6].

2.4.5 Benchmark V: Moving Cylinder

One of the advantages of volume penalization is the ability to easily model moving and deformable obstacles. In order to demonstrate CBVP for moving obstacles, external flow around a cylinder is considered in stationary and moving inertial reference frames. For both cases, the flow parameters remain the same, namely $Ma = 0.1$ and $Re = 185$, where the reference velocity is the difference between the cylinder and freestream. They use an effective resolution of $\Delta x = \Delta y = 1/512$, and penalization parameters $\eta_b = 10^{-2}$ and $\eta_c = 10^{-1}$. The stationary inertial frame is solved on a domain] $\Omega = [-7, 12] \times [-7, 7]$, proceeding until steady periodic vortex shedding is established.

In the moving reference frame, the freestream velocity is halved with respect to the computational grid and the obstacle translated upstream and an equal rate. The result is an inertial frame moving at $u_{\text{inf}}/2$ in the positive x-direction compared to the stationary case. This case is solved on a domain $\Omega = [-22, 7] \times [-7, 7]$ with the same effective resolution. Due to limitations on the total simulation time that are imposed by the domain length, a statistically steady state was unable to be verified. However, comparison of the transient force coefficients C_L and C_D in Figure 2.9 show excellent agreement between late periodic shedding in the moving frame and the statistically steady shedding in the stationary frame.

2.5 Conclusions

A new volume penalization method has been introduced here to extend Brinkman penalization to generalized Neumann and Robin conditions for hyperbolic and parabolic equations. This is accomplished through hyperbolic penalization terms whose characteristics point inward along the surface-normal direction. The process of prescribing BC's is flexible, and constructing problem-specific schemes is systematic through penalization of native variables and propagating to the integrated equations. Multiple approaches to evolutionary boundary conditions, such as the treatment of the density for compressible flows, were developed using CBVP. Such quantities can be

either actively modeled and the physics matched at the solid-fluid interface, or evolved passively making full use of the hyperbolicity of CBVP to propagate physical derivatives.

As with Brinkman penalization, the error of CBVP was shown to be rigorously controlled through the penalization parameter, η. The error from penalized Neumann and Robin Conditions converges as $O(\eta_c)$. With a more favorable convergence than the Brinkman-based penalized Dirichlet condition, which converges as $O(\eta_b^{1/2})$, application to the compressible Navier-Stokes equations typically found the accuracy to be dependent upon the error of the no-slip condition and insensitive to Neumann parameters. In this way, a comprehensive method of imposing general boundary conditions is introduced without significantly impacting the error vis-à-vis the well-vetted Brinkman penalization. The higher order error of CBVP is especially important considering the additional stiffness that accompanies the hyperbolic terms.

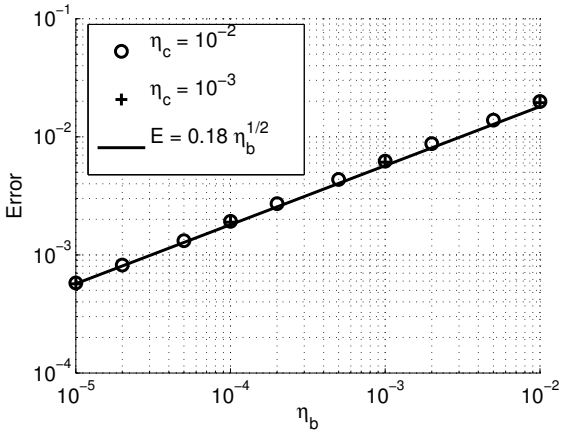

Figure 2.3: L_2-norm error of a fully reflected pulse where η_c is held constant.

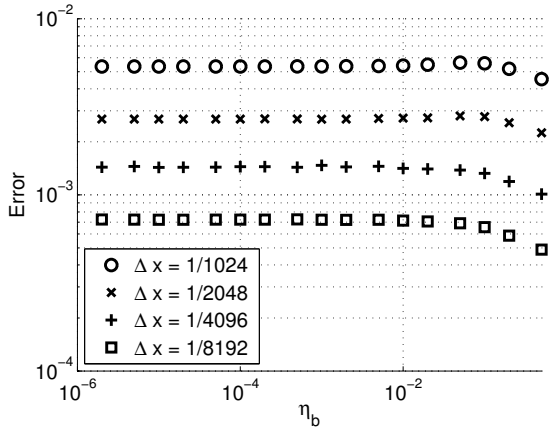

Figure 2.4: L_2-norm error of a fully reflected pulse where numerical viscosity within the obstacle is $\nu_n = \alpha^2 \Delta x^2 / \eta_b$. With $\nu_n = f(1/\eta_b)$, the error demonstrates an insensitivity to the penalization parameter, but is rather controlled by the resolution as $O(\Delta x)$.

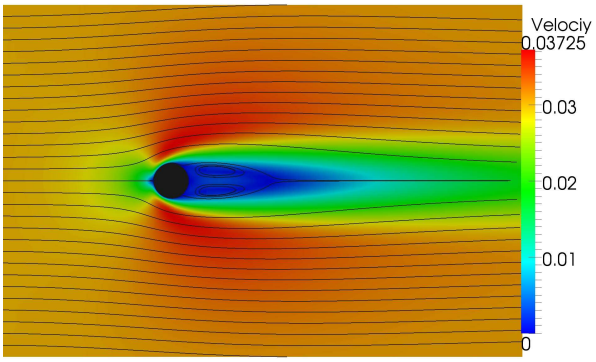

Figure 2.5: Velocity magnitude and streamlines at steady state for $Re = 40$ and $Ma = 0.03$.

	Θ	L	C_D
Experimental			
Coutanceau and Bouard [14]	53.8°	2.11*	−−
Tritton [69]	−−	−−	1.54
2D Numerical			
Linnick and Fasel [40]	−−	2.28	1.54
Dennis and Chang [20]	53.8°	2.35	1.52
Fornberg [25]	55.6°	2.24	1.50
de Tullio et al. [19]	53.7°	2.23	1.49
Present			
$\Delta x = \frac{1}{256}$	**51.6°**	**2.31**	**1.47**
$\Delta x = \frac{1}{512}$	**52.8°**	**2.31**	**1.48**
$\Delta x = \frac{1}{1024}$	**53.7°**	**2.30**	**1.48**
$\Delta x = \frac{1}{2048}$	**53.6°**	**2.28**	**1.51**

Table 2.1: Numerical results for incompressible/pseudo-incompressible flow past a 2D cylinder at $Re = 40$. The separation point Θ and drag coefficient C_D from a CBVP obstacle can be seen converging to previously established results as grid spacing, and therefore nonphysical viscosity, are reduced. The far field flow, as indicated by the separated wake length, is largely unaffected. Note that the wake length L determined by Coutanceau and Bouard [14] is extrapolated at $Re = 40$.

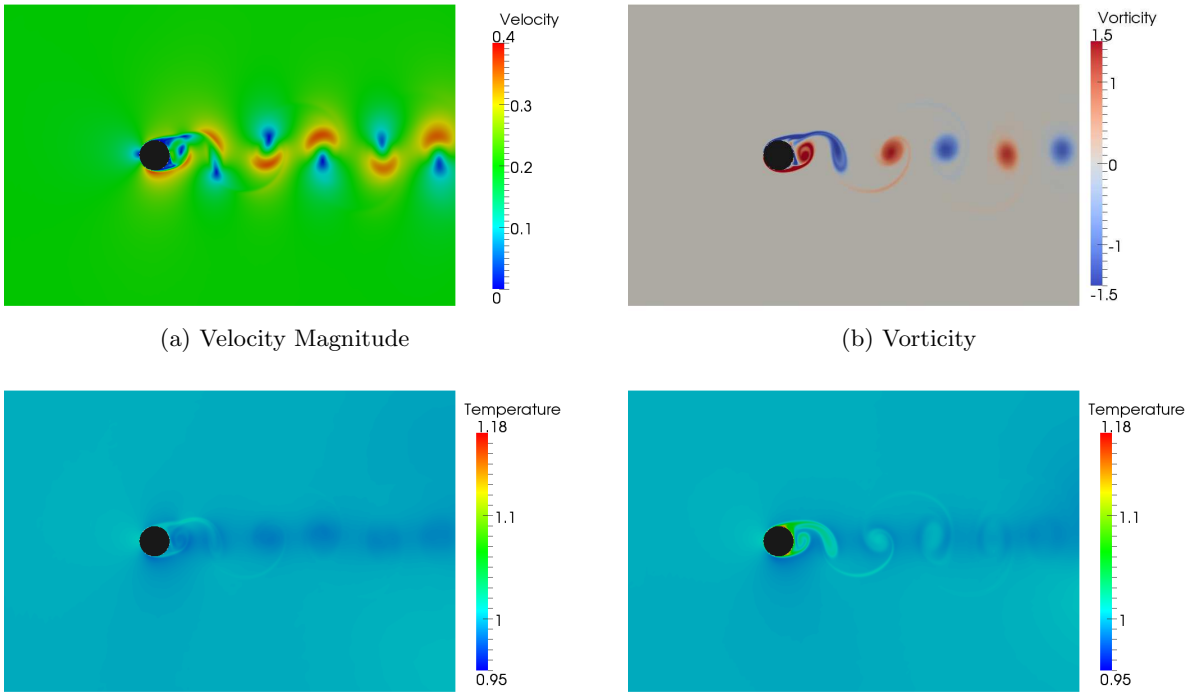

(a) Velocity Magnitude

(b) Vorticity

(c) Temperature - Adiabatic

(d) Temperature - Heated

Figure 2.6: Velocity (2.6a) and vorticity (2.6b) field for flow around an adiabatic cylinder at $Re = 1000$. The Kàrmàn vortex street is clearly visible. The temperature fields are also shown for an adiabatic (2.6c) and heated (2.6d) cylinder, where the nondimensional heat-flux is $q = 1.5$.

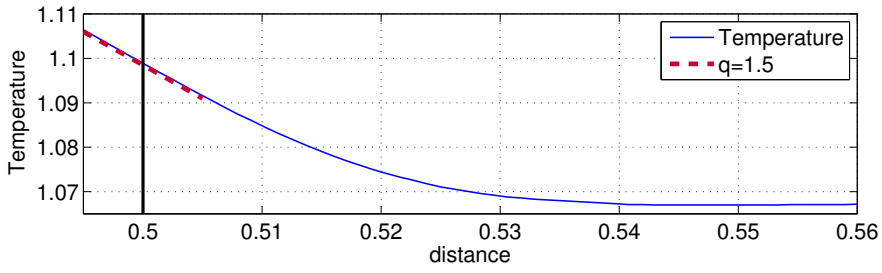

Figure 2.7: Temperature profile along the surface normal at $\theta = \pi/4$, measured from the trailing edge. The imposed Neumann condition $\partial T/\partial \mathbf{n} = q = 1.5$ has been penalized at the surface. The distance along the profile is measured from the center of the cylinder, where the surface is at 0.5.

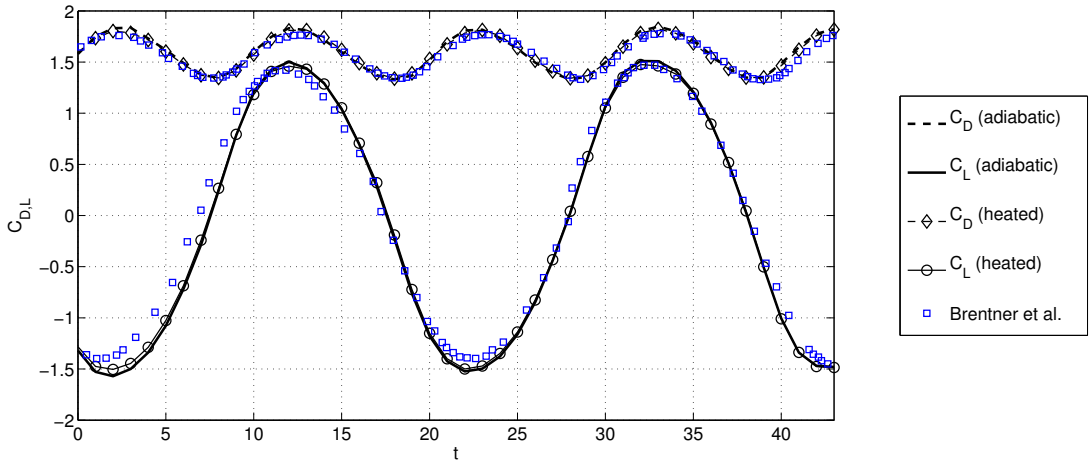

Figure 2.8: Lift and drag coefficients, C_L and C_D, for unsteady flow at $Re = 1000$ compared to those of Brentner et al. [6]. The results presented here agree well, however a slight discrepancy can be seen in a slightly higher shedding frequency.

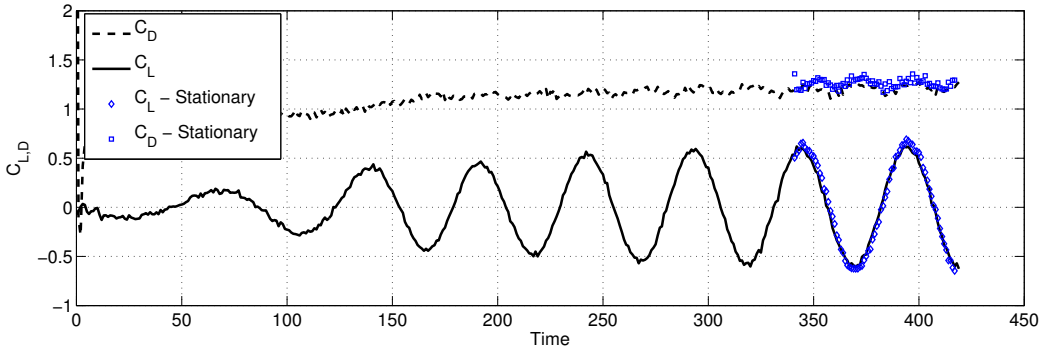

Figure 2.9: Lift and drag coefficients, C_L and C_D, for flow around a impulsively started moving cylinder at $R = 185$. The statistically steady force coefficients for the case solved in an inertial frame of a stationary obstacle are shown for comparison, once periodic shedding is established.

Chapter 3

Adaptive-Anisotropic Wavelet Collocation Method on General Curvilinear Coordinate Systems

3.1 Introduction

The adaptive wavelet collocation method (AWCM)[76] is a powerful tool for computational solutions of parabolic [70], elliptic [72], and hyperbolic [56] partial differential equations, as it allows highly efficient use of memory resources and rigorous control of discretization error. It dynamically adapts the grid using a wavelet basis decomposition to track localized structures in the solution, exploiting spatio-temporal intermittency to optimize the total grid point count. As a result, AWCM has been used to effectively analyze many physical problems, including turbulence [30, 47, 15], reacting flows [57, 51], and geophysics [37].

There are two major deficiencies inherent to AWCM, however, that have limited its application: 1) the "curse of anisotropy," whereby homogeneous wavelet refinement is unable to introduce a spatially varying aspect ratio of the mesh elements and 2) the reliance on a rectangular domain [13]. The first limitation is related to the adaptive mechanism used by AWCM to analyze and refine the mesh, which is isotropic in nature. It is unable to distinguish and exploit highly correlated directions in a variable field where the solution is changing less rapidly than in other directions. Such features, like flame sheets or interfaces, have anisotropic resolution requirements which permit coarser tangential discretization. Wavelet-based adaptation is unable to efficiently exploit these highly correlated and oriented structures. With the associated isotropic adaptation mechanism, increased refinement for gradients in a single direction triggers refinement in all di-

rections irrespective of the need. These filament- and sheet-like structures consequentially become over-resolved, severely degrading the benefits of dynamic adaptivity.

The second limitation is that the use of efficient tensorial wavelets, such as a second generation wavelet basis [62], imposes the requirement for a rectilinear grid. This impedes the efficient application of AWCM towards problems involving complex geometries. In these cases, volume penalization methods have been employed to impose arbitrarily-shaped boundaries [71, 36, 9, 41]. They are simulated through additional forcing terms on the continuous governing equations in nonphysical regions of the computational domain. While this approach circumvents the limitation of the grid topology, it comes with severe drawbacks, among which the most serious are a) approximate nature of boundary conditions, even with guaranteed a priori prescribed accuracy convergence, b) higher surface-normal resolution requirements, c) increased computational stiffness related to penalization terms, and d) additional computational cost associated with the penalization points within the nonphysical volume.

While alternative immersed boundary methods might bypass some of the difficulties associated with volume penalization, all of these approaches ultimately introduce surfaces into the AWCM domain, and therefore suffer from the previously mentioned costs associated with isotropic refinement. Figure 3.1 shows a cross-section from the unsteady flow around a cylinder modeled with the characteristic-based volume penalization method [9]. Due to the solid interface and the high velocity gradient in the boundary layer, the mesh has adapted to the highest permitted level. While the resolution is appropriate in the wall-normal direction, it is excessive in the tangential. Refinement in this manner means that the number of points required to capture surface effects increases with the inverse square of the characteristic normal lengthscale, δ_N, (the viscous boundary layer thickness) and the surface area S, resulting in the computational cost scaling as $O\left(S/\delta_N^2\right)$ in three dimensions. This quickly becomes prohibitive in many applications, such as high Reynolds number wall-resolved turbulent regimes or geometries with a large surface area.

Structured curvilinear meshes reconcile this need for anisotropic refinement with the topological limitations of adaptive wavelet grids. A flexible physical space mesh can be mapped to a

regular rectilinear geometry in a computational space where AWCM can be implemented. For the purposes of this paper, the *mesh* is defined as the geometry of the physical-space discretization, while the *grid* is the structured, rectilinear assembly of collocation points defining the discrete topology and the computational space.

The use of curvilinear coordinate systems to leverage more optimal discretization is a well established approach for solving PDEs [e.g., 67, 53] on nonadaptive grids. Features that are stationary and spatially straightforward to predict, such as boundary layers, benefit from the flexibility of curvilinear mappings to locally and anisotropically control resolution. Additionally, enabling body fitted meshes obviates the need for immersed boundary approaches in many cases.

While it may seem that the use of static anisotropic structured meshes is antithetical to the automated refinement of AWCM, their hybrid implementation is complimentary. Curvilinear meshes provide a continuous mapping that defines local anisotropy and yields a more optimal discretization. On the other hand, a rectangular computational space permits the native implementation of AWCM, which locally refines the grid based on structures in the transformed solution, guaranteeing the accuracy of the solution and quality of the computational grid automatically and *a priori*. This property of solution assurance, irrespective of mesh geometry, is a distinguishing feature of A-AWCM. The coordinate transform then benefits the discretization by reducing the computational cost. Well constructed curvilinear mappings normalize anisotropy in the transformed field variables, permitting more efficient wavelet-based compression into a sparse data representation. The mapping fields themselves are maintained on the grid as additional variables so that AWCM ensures sufficient support to maintain transform operations at a consistent accuracy and, thus, the mesh quality.

In this paper, the general framework for an integrated Adaptive-Anisotropic Wavelet Collocation Method (A-AWCM) is described using curvilinear coordinates. Advantages over isotropic and static mesh optimization are demonstrated by implementing structured curvilinear meshes based on explicit analytic mappings. This approach, however, is presented as a fully general framework that can be implemented with a variety of meshing approaches, including the use of automated

elliptic mesh generation [e.g., 80, 67, 68, 66, 34] as well as spatio-temporally evolving geometries [e.g., 65]. Assurance of consistent global accuracy through the dynamic local refinement of AWCM permits especially flexible use of redistribution and mapping algorithms. Even though the proposed framework is general and highly flexible, the development of automated meshing and anisotropic refinement based on the solution, statistical quantities of interest, and/or for geometries with moving and deformable boundaries is outside of the scope of this paper and left as the subject of future research.

3.2 Adaptive Wavelet Collocation Mesh Refinement

The adaptive wavelet collocation method is a generalized approach for compressing discrete data fields into sparse grid representations. It uses multiresolution analysis to dynamically adapt and refine local resolution to form grids that are suitable for the time-accurate solutions of PDEs.

A spatially dependent field, $u(\mathbf{x})$, is discretized onto a set of dyadic, nested grids and decomposed as

$$u(\mathbf{x}) = \sum_{\in \mathcal{L}^0} c^0 \phi^0(\mathbf{x}) + \sum_{j=1}^{j_{\max}} \sum_{\mu=1}^{2^n-1} \sum_{\mathbf{k}\in\mathcal{K}} d_{\mathbf{k}}^{\mu,j} \psi_{\mathbf{k}}^{\mu,j}(\mathbf{x}), \tag{3.1}$$

where c^0 and $d_{\mathbf{k}}^{\mu,j}$ are the respective coefficients on scaling functions $\phi^0(\mathbf{x})$ and wavelet basis function, $\psi_{\mathbf{k}}^{\mu,j}(\mathbf{x})$. Multidimensional wavelet families, μ, arise from the tensorial product of one-dimensional wavelet and scaling functions, as defined on alternating grid points in each axis-major direction[76]. The resolution levels are identified by level j, where the higher are more refined. Each wavelet has localized wavenumber and spatial support. It is uniquely identified and corresponds one-to-one with the grid points given by $\mathbf{k}$ and .

The sparse grid is created by filtering out collocation points whose wavelet coefficient falls below a prescribed threshold. The coefficients are effectively set to zero, and the corresponding points are discarded. The resulting approximation, denoted $u(\mathbf{x})_{\geq}$, is given by a subset of the

original wavelet basis,

$$u(\mathbf{x})_{\geq} = \sum_{\in \mathcal{L}^0} c^0 \phi^0(\mathbf{x}) + \sum_{j=1}^{j_{\max}} \sum_{\mu=1}^{2^n-1} \sum_{\substack{\mathbf{k}\in\mathcal{K} \\ |d_{\mathbf{k}}^{\mu,j}| \geq \varepsilon \|u\|}} d_{\mathbf{k}}^{\mu,j} \psi_{\mathbf{k}}^{\mu,j}(\mathbf{x}), \tag{3.2}$$

consisting of the dominant information containing modes. Typically, a relative filter threshold ε is used together with the absolute thresholding scale $\|u\|$. This characteristic amplitude scale is often taken as either the L_2- or L_∞-norm of the field u or a derived quantity of interest, such as the Reynolds averaged fluctuating component, $u - \overline{u}$, for turbulent flows. The reconstruction error incurred through the wavelet filtering operation can be shown to be [21]

$$\|u_{\geq} - u\| \leq O(\varepsilon \, \|u\|). \tag{3.3}$$

For a sparse dataset, often a weighted norm of $u(\mathbf{x})$ is taken as the characteristic variational scale, since a strict L_2 norm across discrete sample points can become locally biased by local grid refinement and therefore unrepresentative. In cases where multiple variable fields are adapted upon, $\mathbf{u}(\mathbf{x}) = \{u_1(\mathbf{x}), u_2(\mathbf{x}), \dots\}$, the grid is taken as the union of the grids filtered for each component where the wavelet thresholds, $\boldsymbol{\varepsilon} = \{\varepsilon_1(\mathbf{x}), \varepsilon_2(\mathbf{x}), \dots\}$, can be prescribed independently for each variable of interest.

As the solution evolves, it is necessary to account for wavelets that might become significant in the next iteration or time step. Therefore, the filtered grid is augmented by nearest neighbors to every active point on the current, next higher and next coarser resolution levels. This is justified by the finite propagation rate of information across the grid, which is determined by the type of PDE and iterative or time integration method. Successively filtering and augmenting steps adaptively refine upon and dynamically track local structures in the signal.

The interpolating-lifted wavelet transform at the core of AWCM is recursively computed for one dimension by

$$d_{\mathbf{k}}^j = \frac{1}{2}\left(c_{2\mathbf{k}+1}^{j+1} - P_{\mathbf{k}}^j\right), \tag{3.4}$$

$$c_{\mathbf{k}}^j = c_{2\mathbf{k}}^{j+1} + \widetilde{P}_{\mathbf{k}}^{j+1}, \tag{3.5}$$

where $c^{j+1}_{2\mathbf{k}+1}$ is a discrete sample of $u(\mathbf{x})$ at the $j+1$ (next finer) resolution level, $d^j_{\mathbf{k}}$ are the details at j level of resolution, $P^j_{\mathbf{k}}$ is the corresponding interpolant taken from coarser nodes on the j level, and $\widetilde{P}^j_{\mathbf{k}}$ is the interpolant from the details on the finer $j+1$ level of resolution. Lagrange polynomial interpolants with finite stencils are used to calculate $P^j_{\mathbf{k}}$ and $\widetilde{P}^j_{\mathbf{k}}$. For many implementations it is common to omit the update step (3.5), especially for distributed memory solvers [49]. The inverse transform is computed simply by applying the algebraic inverse of (3.4-3.5), starting from the coarsest resolution level. As new nodes are added during mesh adaptation, the solution is interpolated to them by explicitly including those collocation points with coefficient $d^{\mu,j}_{\mathbf{k}} = 0$ and performing the inverse transform operation. Finite differencing is used to calculate derivative approximations, for which wavelet interpolation provides stencil support for collocation points not included in the sparse, filtered grid in (3.2).

Multidimensional wavelets are the tensorial product of their 1D counterparts, therefore the multidimensional transform is taken by consecutive application of (3.4-3.5) across every direction, and recursively for each resolution level. While the wavelet basis functions for some multidimensional families, μ, are anisotropic in a strict sense, they cannot be exploited for anisotropic refinement as they result from the lifting transform itself. The families are a direct consequence of the discrete location on the collocation grid; furthermore, the shapes align with the rectilinear axes. Since AWCM tightly integrates mesh adaptation, interpolation, and the computational environment, attempting to impose an artificial anisotropic refinement method externally would introduce excessive artifacts by violating the consistency of the wavelet-space representation. Restricting refinement is equivalent to discarding significant information-carrying modes from the perspective of the wavelet filter, (3.2). This discrete damping is unlike the action of the filter thresholding in that its effects are unbounded. In such a case, summation across the wavelet basis would no longer form a valid approximation for the original signal $u(\mathbf{x})$ at the *a priori* threshold level. Even if such additional processing of the grid were tenable, the geometry only permits anisotropic control in the major axis directions.

Despite this shortcoming, tensorial lifted-interpolated wavelets are highly desirable for the

solution of PDEs due to their simplicity and computational efficiency, as the transform (3.4-3.5) can be accomplished in $O(N)$ operations.

3.3 Adaptive-Anisotropic Wavelet Collocation Method Framework for Curvilinear Meshes

The Adaptive-Anistropic Wavelet Collocation Method circumvents the shortcomings of the wavelet transform by employing the general framework for a harmonic mesh map [e.g., 22], which maps the physical domain $\Omega_p(\mathbf{x})$ to the computational domain $\Omega_c(\boldsymbol{\xi})$ (both assumed to be Riemannian manifolds):

$$\boldsymbol{\xi}(\mathbf{x}) : \Omega_p \rightarrow \Omega_c, \boldsymbol{\xi} = (\xi_1, \xi_2, \xi_3), \mathbf{x} = (x_1, x_2, x_3). \tag{3.6}$$

This allows for flexibility of the mesh geometry and more optimal point distribution by partially decoupling the physical mesh from the natural coordinate system implied by the rectilinear computational grid. Spatially varying cell aspect ratios and orientation, including body fitting, can then be prescribed within the physical domain, Ω_p, based on the problem being solved. This mesh is mapped back onto a rectilinear grid, which is suitable for the discrete operators, including the wavelet transform and derivative approximations.

Assuming that the final mesh is well conditioned and of sufficient quality to support the discrete PDE solution, this approach is agnostic to the methods that are used to construct it. Explicit, analytic curvilinear mappings are sufficient for the theoretical consideration of this general framework, though their use is limited for applied problems of engineering interest. In such cases, more advanced mappings and automated generation methods, either continuous or discrete, would prove more useful.

Transform between the Cartesian physical space basis, $\{\mathbf{e}_1, \mathbf{e}_2, \mathbf{e}_3\}$, and the computational curvilinear basis, $\{\mathbf{b}_1, \mathbf{b}_2, \mathbf{b}_3\}$, proceeds as

$$\mathcal{J}_{ij}\mathbf{e}_i = \mathbf{b}_j, \tag{3.7}$$

where $\boldsymbol{\mathcal{J}}$ is the Jacobian matrix,

$$\mathcal{J}_{ij} = \frac{\partial x_i}{\partial \xi_j}, \tag{3.8}$$

and summation is implied across indices.

Given that the computational grid is rectilinear, the unmodified AWCM approach is directly implemented, where it adapts and refines the grid upon the transformed solution fields $\mathbf{u}(\boldsymbol{\xi})$. The inverse coordinate mappings $\mathbf{x}(\boldsymbol{\xi})$, which define the physical mesh geometry and support the discrete version of (3.7), are likewise tracked. The Jacobian matrix $\mathcal{J}_{ij}$ is therefore readily computed from these mappings using the integrated finite difference framework. For the construction of PDE terms, which are naturally prescribed in physical space, computational derivative approximations are calculated as

$$\frac{\partial}{\partial x_j} = \mathcal{J}^{-1}_{ji} \frac{\partial}{\partial \xi_i}, \tag{3.9}$$

where $\mathcal{J}^{-1}_{ji}$ is the inverse Jacobian matrix.

Adapting upon the coordinate mappings, $\mathbf{x}(\boldsymbol{\xi})$, with a low, independent wavelet threshold, $\varepsilon_{\mathbf{x}}$, ensures consistent accuracy of transformation operations, and automatically controls the quality of the sparse representation of the mesh. Spurious artifacts can otherwise arise if the local accuracy of the discrete Jacobian matrix approximation (3.8) deteriorates as a result of grid coarsening.

On the transformed solution, $u(\boldsymbol{\xi})$, the wavelet filter maintains *a priori* accuracy of the L_2- and L_∞- norm in the usual manner following (3.3). Given that the transform of u is purely spatial, the corresponding L_∞-norms are equal,

$$\left\| u(\boldsymbol{\xi}) - u(\boldsymbol{\xi})_{\geq} \right\|_\infty = \left\| u(\mathbf{x}) - u(\mathbf{x})_{\geq} \right\|_\infty . \tag{3.10}$$

Furthermore, the L_2-norms can be shown to be equivalent, as $\int_{\Omega_p} f(\mathbf{x}) d\mathbf{x} = \int_{\Omega_c} f(\mathbf{x}(\boldsymbol{\xi})) \mathcal{J}(\boldsymbol{\xi}) d\boldsymbol{\xi}$. Therefore, error convergence of the physical space solution, $u(\mathbf{x})$, which is of primary interest, is likewise guaranteed by (3.3).

Local anisotropic refinement and unidirectional stretching of the physical space mesh is introduced by adjusting the location and distribution of points through the definition of the coordinate mappings, $\mathbf{x}(\boldsymbol{\xi})$. This compliments wavelet-based adaptation, which adjusts the local mesh point

density but preserves the underlying geometry and local aspect ratio of the physical mesh. With properly constructed meshes, highly correlated gradients in physical space become normalized once transformed to computational space. This results in more efficient isotropic refinement through AWCM, a smaller memory footprint, and a more optimal use of computational resources. However, since accuracy convergence through AWCM is unified in both spaces, Ω_p and Ω_c, the solution *fidelity* is independent of the anisotropic refinement. With this general decoupling of the accuracy from the mesh geometry, A-AWCM is more robust and flexible than nonadaptive structured meshes. Note that this property is contingent upon a well conditioned geometry that is capable of numerically supporting the transform operations. High skewness, degenerate Jacobian matrix ($\mathcal{J} \rightarrow 0$), and non-smooth mesh lines can cause a degradation of the transform operations (3.7) that can not be compensated for by wavelet grid refinement. One consequence of solution/geometry independence is that it essentially eliminates the need for traditional *a posteriori* mesh convergence studies to guarantee the solution quality. Furthermore, it provides enormous robustness and flexibility for moving mesh [e.g., 65] and mesh redistribution [e.g., 64] methods for time-marching integration schemes, as AWCM will preserve the solution if the mesh geometry becomes temporarily sub-optimal.

In general, well constructed mapping fields, $\mathbf{x}(\boldsymbol{\xi})$, can be provided by a variety of means. In the simplest configurations and with *a priori* understanding of the solution field, explicit algebraic functions can impose body fitting and provide some anisotropic benefit to the computational cost. More complex problem geometry and more optimal mesh distribution are typically achieved through automated methods, including the solution of elliptic or hyperbolic PDEs [67, 66, 34]. Many approaches involve dynamic redistribution and moving meshes [65], either as a cost optimization or to capture moving/deformable geometry. Development of automatic meshing, mesh redistribution, and anisotropic refinement methods that exploit the particular computational environment and take advantage of A-AWCM are a topic of future research.

Each time the grid is dynamically refined through the wavelet mechanism, the mesh must be updated with the physical space positions of the new points in the discrete mapping. Added

nodes are treated in one of two ways, depending on how the mesh is explicitly defined. For meshes that are exactly defined at every potential grid point, either through the deterministic solution of an equation (e.g. algebraic or PDE) or some other procedural method, the mapping must be consistently prescribed for every point that is introduced. Fully discrete maps must have some mechanism for updating grid points, such as a multiresolution nested definition or the ability to be refined at will. For some methods, this can involve a potentially expensive global/iterative solution that can add substantial cost to the refinement. Alternatively, the mesh can be strictly defined by the continuous, static wavelet representation $\mathbf{x}_{0,\geq}$ of any arbitrary mapping, $\mathbf{x}_0$, filtered to a fixed subset of nonzero wavelet basis functions $\mathcal{K}_0 \subset \mathcal{K}$. From this, the value of the map (and thus the physical coordinate) of a new points at any location in Ω_p is interpolated from $\mathbf{x}_{0,\geq}$ using the wavelet transform. The subset, $\mathcal{K}_0$, of wavelet functions at grid points and the coefficient values are determined by an initial mesh generation step, and retained throughout the course of solution. For static geometries, this has the ability to amortize the cost of highly sophisticated generation methods and to ensure that grid refinement will maintain a piecewise-smooth mesh suitable for the polynomial-based numerical framework. It should be noted that the adaptive wavelet filter is not positive preserving, so care must be taken to ensure that the continuous field $\mathbf{x}_{\geq}$ is monotonic to within a tolerance specified by the finest mesh resolution. This can be enforced by AWCM in the usual manner.

3.4 Numerical Results

The A-AWCM framework is fully general for the solution of elliptic, parabolic and hyperbolic PDEs. In order to demonstrate the central principles of the method, it has been applied and examined here for parabolic and hyperbolically dominant cases. Corresponding mesh geometry includes body fitting and the introduction of local anisotropy to match general trends in the solution. This is shown to optimize dynamically adaptive meshes while retaining the fidelity control and error convergence inherent to AWCM.

While sophisticated meshing techniques can be employed, analytic mappings are used in these

cases for simplicity and to highlight the general framework and demonstrate the concepts of A-AWCM, namely the implementation of spatially inhomogeneous anisotropic meshes, h-refinement in arbitrary geometries, and rigorous error control. Development of automated meshing techniques that exploit this framework is left as a topic for future research.

The cases considered here are parabolic diffusion, acoustic scattering, and unsteady external compressible viscous flow. While AWCM, and by extension A-AWCM, can be implemented with arbitrary order wavelets and finite-differences [72], all of the results shown here use 4-th order for both.

3.4.1 Parabolic Diffusion

Time-accurate parabolic diffusion is examined on a 2D rectangular domain, defined by the physical bounds $\mathbf{x} \in [0, \pi] \times [0, \pi]$. A nonhomogeneous profile of the diffusive scalar, u, is imposed along one edge, generating a steep initial gradient that drives diffusion into the domain.

The parabolic diffusion equation is defined in physical space as

$$\frac{\partial u}{\partial t} = \frac{\partial}{\partial x_j}\left(\kappa \frac{\partial u}{\partial x_j}\right), \tag{3.11}$$

where the diffusion coefficient used here is constant, $\kappa = 1$. In order to be solved, it is transformed into the computational coordinates as

$$\frac{\partial u}{\partial t} = \mathcal{J}_{ji}^{-1}\frac{\partial}{\partial \xi_i}\left(\kappa \mathcal{J}_{ji}^{-1}\frac{\partial u}{\partial \xi_i}\right). \tag{3.12}$$

It should be noted that this transform is fully procedural and can be easily abstracted, minimizing the cost of implementation in existing codebases.

The boundary conditions are given as

$$\left.\frac{\partial u}{\partial x}\right|_{x=0,\pi} = 0, \tag{3.13}$$

$$u|_{y=0} = 0, \tag{3.14}$$

$$u|_{y=\pi} = f(x), \tag{3.15}$$

where the Cartesian coordinates $\mathbf{x} = (x, y)$ will be used interchangeably with $\mathbf{x} = (x_1, x_2)$ for simplicity of the discussion. This convention is used hereafter.

A fifth order polynomial is specified for $f(x)$. The initial condition is defined by the series

$$u|_{t=0} = \sum_m \left[A_m \frac{\sinh(my)}{\sinh(m\pi)} + \sum_n C_{m,n} \sin(ny) \right] \cos(mx), \tag{3.16}$$

where the expansion coefficients A_m, and $C_{m,n}$ are computed to match the boundary conditions, (3.13-3.15), and an initial steep exponential decay in the y direction. This provides a smooth approximation of an impulsive perturbation at the $y = \pi$ edge, generating a steep gradient in the transported scalar.

The grid is given by a base mesh of $N = [5 \times 5]$ points, with $j_{\max} = 10$ levels of resolution, yielding equivalent, nonadaptive resolution of $N_{\max} = [2049 \times 2049]$. The physical mesh is intentionally non-tensorial and introduces skewness to demonstrate the generality of the method. An algebraic curvilinear, two-dimensional coordinate mapping, $\mathbf{x} = \{x, y\}$, define the mesh across the computational domain $\boldsymbol{\xi} = \{\xi, \eta\} \in [0, \pi] \times [0, \pi]$ as

$$x = \phi \left[\frac{-1.9}{\pi^2} \xi^3 + \frac{2.85}{\pi} \xi^2 - 0.95\xi \right] + (1 - \phi)\, \xi, \tag{3.17}$$

$$y = \frac{-0.65}{\pi^2} \eta^3 + \frac{0.45}{\pi} \eta^2 + 1.1\eta, \tag{3.18}$$

where a blending function controls the local expression of x-direction anisotropic stretching,

$$\phi = \frac{-2}{\pi^3} \eta^3 + \frac{3}{\pi^2} \eta^2. \tag{3.19}$$

The full grid at the $j = 3$ resolution level is illustrated in Figure 3.2. This mesh has been stretched in the y-direction to more efficiently resolve the steep initial gradient that is formed on the $y = \pi$ edge at early timesteps. The mild stretching in the x-direction near the perturbed edge captures some of the variability in the boundary profile, $f(x)$. In comparison, a standard isotropic wavelet grid in Figure 3.3 shows increased refinement in the corners resulting from the initial temperature field and the one-sided interpolating stencils near the grid edges.

It should be noted that this particular mesh has been generated to approximate general trends in the solution, but has not been intentionally or optimally constructed to capture the functional form of the initial conditions, as wavelet refinement provides any additional refinement and automatically filters out over-resolved regions.

The error convergence at $t = 0.05$ is shown in Figure 3.4. As with the standard rectilinear implementation, both the physical space L_2- and L_∞-norm are well controlled and scale with the adaptive wavelet threshold parameter as $O(\varepsilon)$. Furthermore, for standard rectilinear AWCM the total number of grid points, $\mathcal{N}$, scales with the wavelet threshold as $O(\mathcal{N}^{-p/n})$, where p is the order of the wavelets and spatial derivative operator and n is dimensionality of the problem [72].

3.4.2 Acoustic Scattering

For an examination of hyperbolically-dominant PDEs, consider the acoustic scattering problem of Tam and Hardin [63]. A low amplitude pulse reflects off of the surface of a cylinder, and is scattered into the far field. Here the cylinder is modeled using a body-fitted O-type mesh with appropriate BCs, obviating an immersed boundary approach.

The fully compressible Navier-Stokes equations

$$\frac{\partial \rho}{\partial t} = -\frac{\partial \rho u_j}{\partial x_j}, \tag{3.20}$$

$$\frac{\partial \rho u_i}{\partial t} = -\frac{\partial}{\partial x_j}\left(\rho u_i u_j + P\delta_{ij} - \sigma_{ij}\right), \tag{3.21}$$

$$\frac{\partial \rho e}{\partial t} = -\frac{\partial}{\partial x_j}\left(\rho u_j (e + P) + u_i \sigma_{ij} - q_j\right) \tag{3.22}$$

are transformed and solved in the curvilinear coordinates in a rectangular computational space, Ω_c, as before.

The energy for the acoustic signal is provided by a small, Gaussian perturbation in the initial condition,

$$u' = p' = 10^{-3} \times 2^{-\frac{(x-c)^2+y^2}{0.04}}, \tag{3.23}$$

superimposed on a quiescent field, centered at $c = 4$. Nonreflective boundary conditions in the far

field are simulated by a characteristic-based buffer region [27], where convective forcing is aligned with the radial direction for computational efficiency.

A high acoustic Reynolds number of $\mathrm{Re}_a = 10^5$, based on the cylinder diameter and far field fluid properties, is used to approximate the Euler equations and match the analytic solution given for an inviscid fluid [63]. Given the finite Reynolds number, the BCs on the cylinder are prescribed to be no-slip and isothermal, resulting in a minute boundary layer forming during the transient interaction between the acoustic pulse and the solid surface. Correspondingly, the mesh is anisotropically refined in the radial direction by the function

$$r = 1 + \frac{\tanh\left(\frac{3}{2}\left(\frac{\xi-\xi_{\min}}{\xi_{\max}-\xi_{\min}} - 1\right)\right)}{\tanh\left(\frac{3}{2}\right)} \tag{3.24}$$

in order to efficiently resolve the steep gradient that will be generated in the wall normal direction. At the cylinder surface, the mesh takes upon a high aspect ratio of $A \approx 4:1$ in physical space, with the first gridpoint at a distance of $r/D \approx 0.00014$ at the highest resolution level. Mesh lines are evenly spaced in the azimuthal direction. The computational grid at maximum resolution is equivalent to $N_{\max} = [3073 \times 5632]$, and utilizes a limit of 10 levels of adaptive refinement, sufficient to fully resolve all simulations without artificial truncation. Figure 3.5 shows the mesh at the $j = 3$ level of resolution. As with the previous problem, only very general and conservative considerations have been taken in construction of this mesh. The use of AWCM ensures that regions of over- or under-resolution will be refined accordingly to optimize the grid for the underlying geometry.

The reflection of the acoustic pulse is shown in figure 3.6 for a threshold of $\varepsilon = 5 \times 10^{-3}$. In the locations of high strain rate at the cylinder surface, the mesh has refined to a high level, while remaining coarser at other surface regions. As an explicit Runge-Kutta method is used for time integration, the small resolved spatial scales severely, though temporarily, restrict the computational timestep, Δt, in order to maintain stability in accordance with the CFL condition. This is limited to a relatively concise window in time when the acoustic pulse interacts with the cylinder.

The structure of the acoustic wave spans a large portion of the domain. In the far field, a greater number of levels of refinement are used to resolve the wave structure. Typically, structured

O-type meshes yield non-uniform fidelity, as the mesh becomes stretched and enlarged as the radius increases, degrading the resolution power and spatial accuracy of derivative approximations. With A-AWCM, however, a uniform accuracy specified by the wavelet threshold, ε, is maintained at all radial locations, provided that there are sufficient adaptive levels, $j_{\max}$, to support the necessary refinement. Figure 3.6b shows an approximation of the local element size across the physical domain. Consistent physical resolution is provided for the wave structure that spans the entire radial distance. The physical mesh geometry, therefore, does not degrade the solution quality. This ability to maintain consistent spatial representation, and therefore globally constant fidelity, is unique to A-AWCM.

Furthermore, A-AWCM is able to exploit transients in the solution. Before and after the period where the main acoustic waves are actively interacting with the solid surface, the strain rate at the surface is negligible, and the mesh is refined only to a coarse level as shown in Figure 3.7. The resulting timestep is then much larger, and only limited by the mesh spacing required to resolve the pulse in the far field.

The pressure at point $\mathbf{x} = (\sqrt{2}, \sqrt{2})$ is shown in 3.8. Both the initial wave and its reflections from the cylinder are visible. As the wavelet threshold is decreased, the error and spurious artifacts in the transient solution can be clearly seen to converge towards the analytic inviscid solution.

3.4.3 External Flow

For unsteady, 2-D flow around a cylinder, the compressible Navier-Stokes equations (3.20-3.22) are solved for $\mathrm{Re} = 250$ at subsonic Mach number $\mathrm{Ma} = 0.1$, where the Reynolds number is based on the inflow velocity, cylinder diameter, and far-field fluid properties. In this configuration, the governing system of PDEs demonstrates both strong parabolic, hyperbolic, and convective effects. While the flow is still laminar at this Reynolds number, a well structured von-Kármán vortex street forms in the cylinder wake.

The computational grid has an equivalent finest resolution of $N_{\max} = [640 \times 384]$, employing 7 adaptive levels. In physical space, an O-type mesh is used, with azimuthal and radial distribution

of mesh points following that of Beaudan and Moin [3]. A more conservative estimation of the wake region is prescribed to ensure that the vortex street is fully resolved. Wavelet-based adaptation compensates for the overly dense mesh geometry. The boundary layer is anisotropically refined using geometric cell growth starting from an aspect ratio of approximately 2.5 : 1 in the radial direction, with the first point from the surface placed at $r/D \approx 0.0032$. The non-adaptive mesh at the $j = 4$ level is shown in Figure 3.9. In order to capture important physical behavior in the solution, the wavelet filter is set to adapt upon momentum, vorticity and the magnitude of the strain rate tensor. Three simulations were run with the normalized wavelet threshold filter set to ranges across $10^{-3} \geq \varepsilon \geq 10^{-1}$.

Time-accurate lift and drag coefficients are shown in Figure 3.10, and the statistical results are summarized in Table 3.1. For the most well refined case, where $\varepsilon = 10^{-3}$, the average drag coefficient ($\overline{C}_D$), RMS of the lift coefficient ($C_{L,RMS}$), and Strouhal number (St) for the shedding frequency agree well with established results [4, 50]. At the higher threshold value of $\varepsilon = 10^{-2}$, indicating discretization error of $O(1\%)$, these low-order statistics are reasonably approximated using only 5.1% of the total grid points. At the highest threshold value, the solution is only very roughly approximated on the nearly coarse grid.

From Figure 3.11b, the advantage of a body fitted mesh with A-AWCM is clearly visible. The resolution is not uniform along the surface, but rather tracks unsteadiness within the boundary layer and optimizing the number of points to resolve separately the stagnation and separation points, and near-wake bubble. There are only very limited regions where the highest resolution level has been reached, indicating that the solution is indeed captured at a numerical accuracy $O(10^{-3})$ without effects from the finite available resolution levels. Furthermore, AWCM exploits the near-surface intermittency of the oscillating shear layer resulting from boundary layer separation. The anistropically stretched elements on the surface reduce the number of refinement levels that are used to resolve much of the boundary layer.

As vortical structures are convected into the far-wake, increasingly higher resolution levels again compensate for the larger cells inherent to O-meshes, maintaining highly accurate spatial

ε	$\overline{C}_D$	$C_{L,RMS}$	St	$\mathcal{R}$
10^{-1}	1.026	0.312	0.195	3.6%
10^{-2}	1.265	0.495	0.201	5.1%
10^{-3}	1.273	0.507	0.204	19.5%

Table 3.1: Computed drag ($\overline{C}_D$) and lift ($C_{L,RMS}$) statistics, Strouhal number (St) and percentage of adaptive points retained ($\mathcal{R}$) for pseudo-incompressible flow around a cylinder at Re = 250 at various values of the wavelet threshold. The values were computed for 15 shedding cycles once the solution had reached statistically steady state.

resolution. While the smallest physical lengthscales are typically found at the surface and in the near-wake, the curvilinear transformation effectively regularizes the regional scales in addition to providing anisotropy for the boundary layer. This allows AWCM to compensate for the underlying stretching and coarsening that occurs in the far-field of O-type meshes without the compounding costs of over-resolving the near region.

3.5 Conclusions

The general framework for A-AWCM leverages the advantages of both curvilinear mesh geometries and wavelet-based adaptive refinement. The use of a transformed coordinate system allows the simultaneous use of complex geometry meshes as well as efficient wavelet algorithms for the solution of parabolic, elliptic, and hyperbolic PDEs. Spatially varying anisotropic and complex geometries can therefore be introduced to more optimally discretize the domain for a given problem, thereby circumventing the deficiencies that accompany the isotropic refinement mechanism of AWCM. This permits greatly reduced computational resources, especially with solutions that contain filament- and sheet-like structures that are often prohibitively expensive for isotropic refinement approaches. Furthermore, this enables AWCM to be used in a body-fitted context for solving applied problems.

Within this framework, many of the most attractive properties of AWCM have been preserved. The grid adapts to track structures in the solution and thereby exploits intermittency to greatly reduce the memory footprint. Fidelity of the physical space solution is rigorously controlled *a*

priori through the wavelet threshold, ε, and error convergence is demonstrated for both the L_2 and L_∞ norms. Furthermore, the accuracy is maintained globally. The adaptive wavelet transform yields uniform spatial discretization in physical space regardless of the underlying mesh geometry, provided that the local mesh structure is well conditioned for transformation operations. This is a unique property of A-AWCM, and largely decouples the mesh geometry from the quality of the solution. The mesh therefore generally implicates only the computational cost and efficiency of the discretization.

While this method has been demonstrated on a series of problems with analytically created meshes, the framework itself is agnostic to the particular generation method. It allows for the use of more sophisticated and automated meshing and mesh redistribution approaches. A high degree of flexibility can be exercised with these methods since a consistent solution fidelity can be guaranteed through the adaptive wavelet mechanism. This implies an optimization of the grid for a given geometry by removing excess grid points in over-resolved regions. Advanced meshing methods that exploit the particularities of the integrated A-AWCM environment are topics of ongoing research.

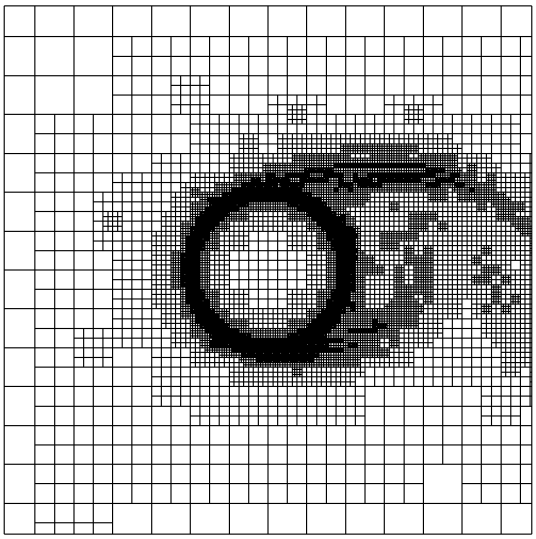

Figure 3.1: The adaptive mesh for the unsteady flow around a cylinder imposed by volume penalization. Isotropic refinement via AWCM has created a very large number of points around the immersed surface and boundary layer.

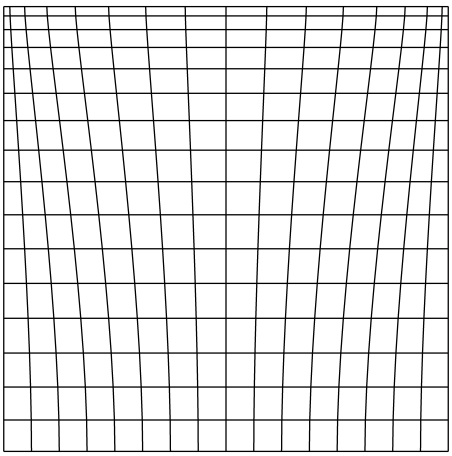

Figure 3.2: The non-adapted mesh at the $j = 3$ resolution level used to solve a parabolic diffusion equation across a square plate. Anisotropic refinement is prescribed on the top boundary to account for steep gradients at early timesteps.

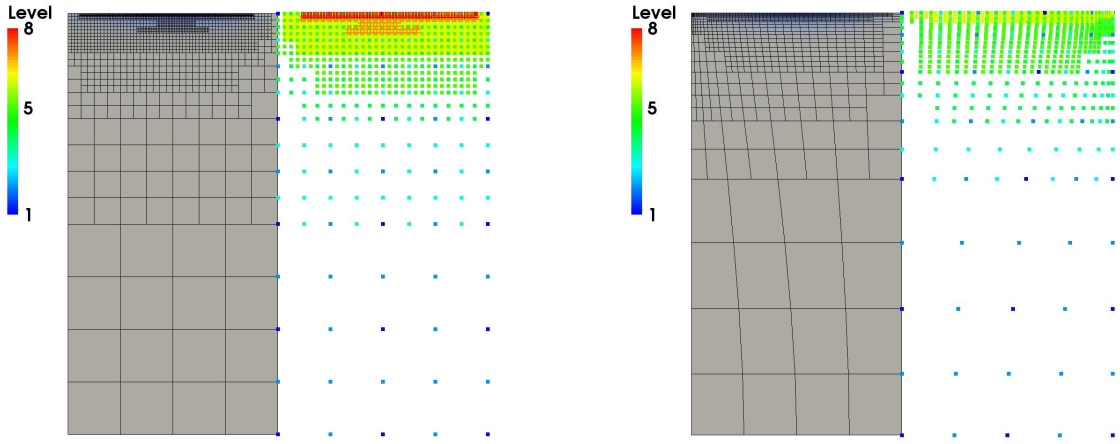

(a) (b)

Figure 3.3: The mesh as adapted upon the initial conditions of u with a steep decay from a quintic polynomial BC. Using the same wavelet threshold, $\varepsilon = 10^{-3}$, the fully rectilinear mesh (a) uses both a greater number of total points and a higher resolution level than the more optimal curvilinear mesh geometry (b).

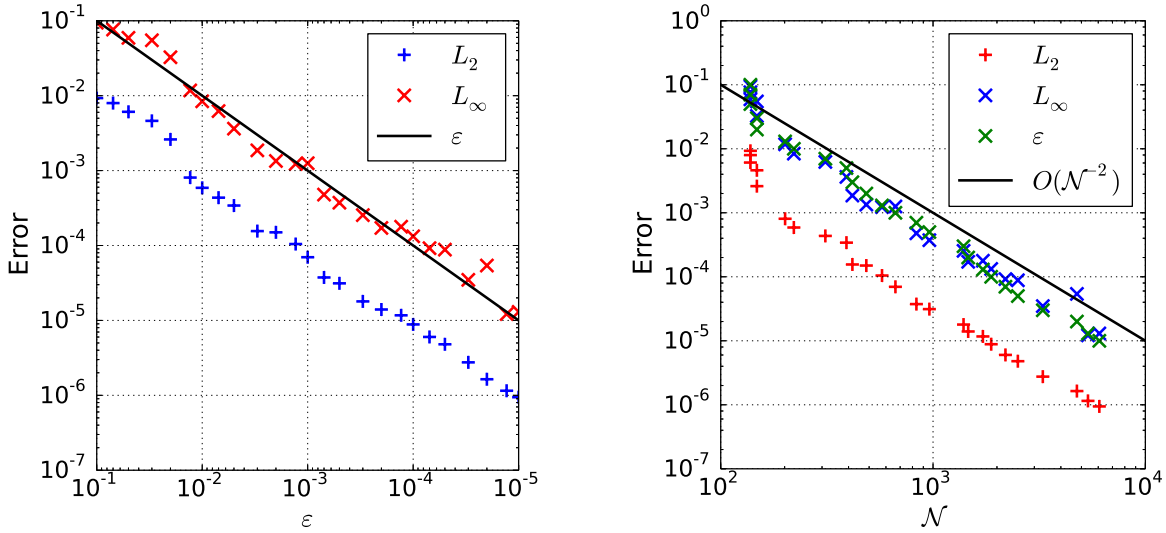

(a) (b)

Figure 3.4: Both L_2- and L_∞-norm errors of the physical-space numerical solution converge linearly with the wavelet threshold parameter, ε. As shown by Vasilyev and Kevlahan [72] for 4-th order wavelets and finite differences, the error and threshold ε scale with the total number of grid points as $O(\mathcal{N}^{-2})$.

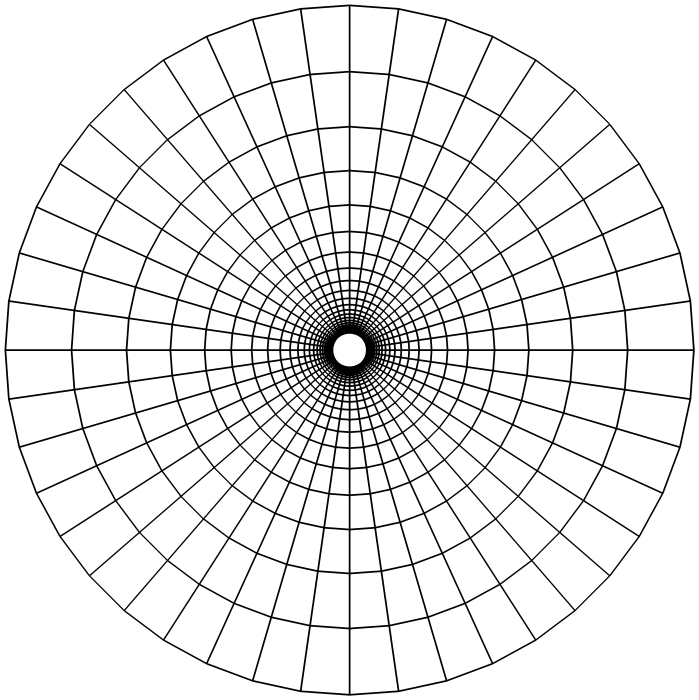

Figure 3.5: An O-type mesh is used to simulate acoustic scattering off of a solid cylinder. The mesh is shown with all gridlines at the $j = 3$ resolution level displayed. Stretching in the radial direction introduces anisotropy in the mesh at the surface of the cylinder in order to more efficiently resolve the boundary layer.

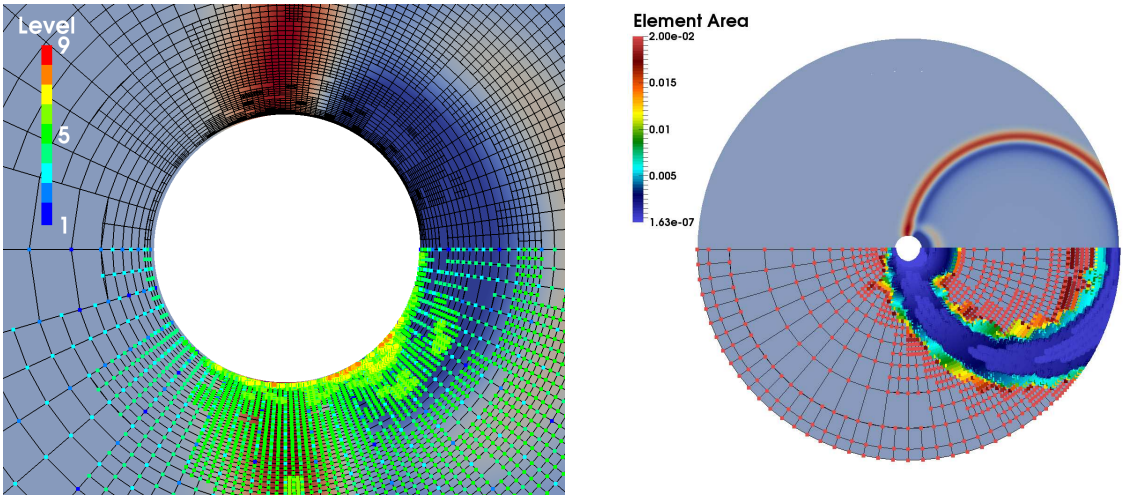

(a) (b)

Figure 3.6: The pressure field at $tD/a = 4$, when the acoustic wave is passing and reflecting off of the surface of the cylinder. The minuscule boundary layer is causing the grid to adapt to the $j = 9$ level with $\varepsilon = 5 \times 10^{-3}$. Examination of the approximate element area shows that uniform resolution is maintained through wavelet-based adaptation across the acoustic pulse, which spans from the cylinder to the far field, regardless of local stretching in the mesh geometry.

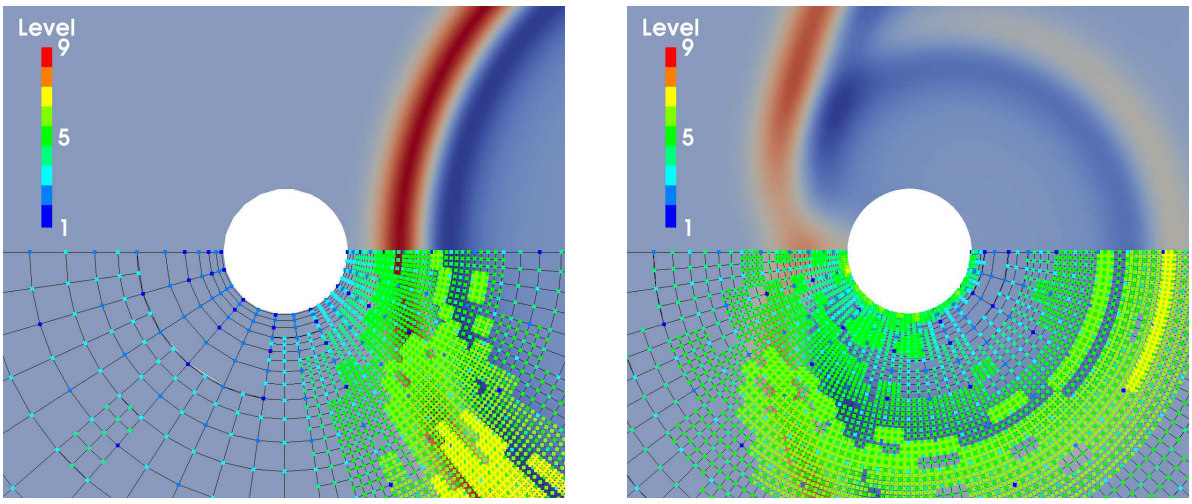

(a) (b)

Figure 3.7: The pressure field and adaptive mesh at $tD/a = 3$ (3.7a) and $tD/a = 5$ (3.7b). When the main pulse is not directly interacting with the cylinder, the grid locally coarsens, thereby relaxing the explicit time step through the CFL condition.

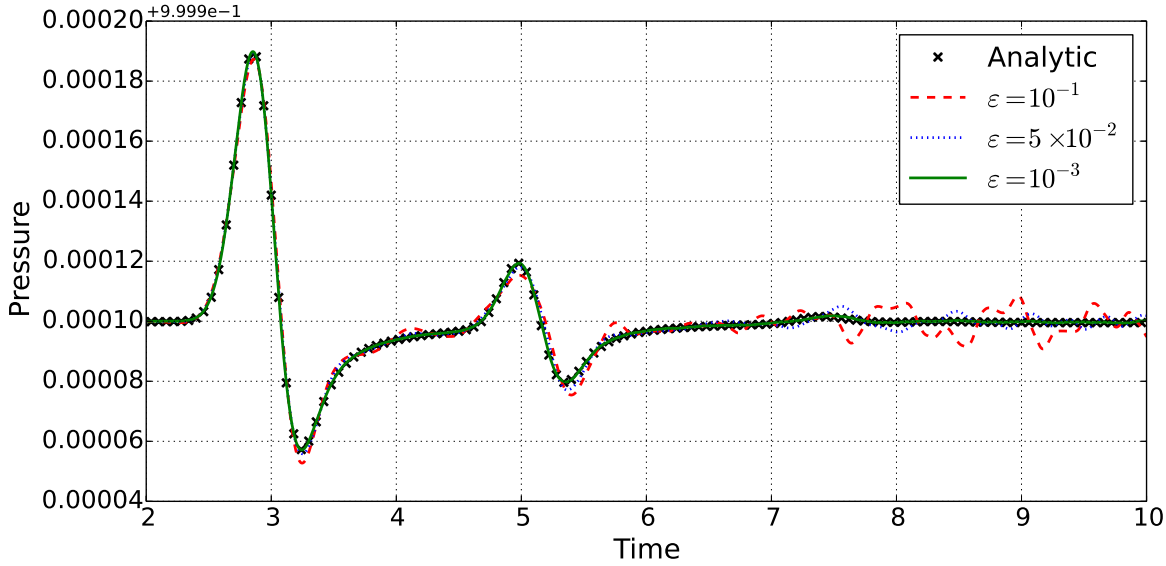

Figure 3.8: Acoustic scattering measured at point $\mathbf{x} = (\sqrt{2}, \sqrt{2})$. The error and numerical artifacts in the reflected wave can clearly be seen to converge as ε decreases. Correspondingly, the percentage of the total nodes retained in the adaptive grid at $t = 4.0$ is $\mathcal{R} = 0.9\%$ and 1.3% for $\varepsilon = 10^{-1}$, and 5×10^{-2}, respectively, which were resolved using 8 resolution levels. Since the case where $\varepsilon = 10^{-3}$, required 10 levels to be fully resolved, a direct comparison of the compression ratios is not possible.

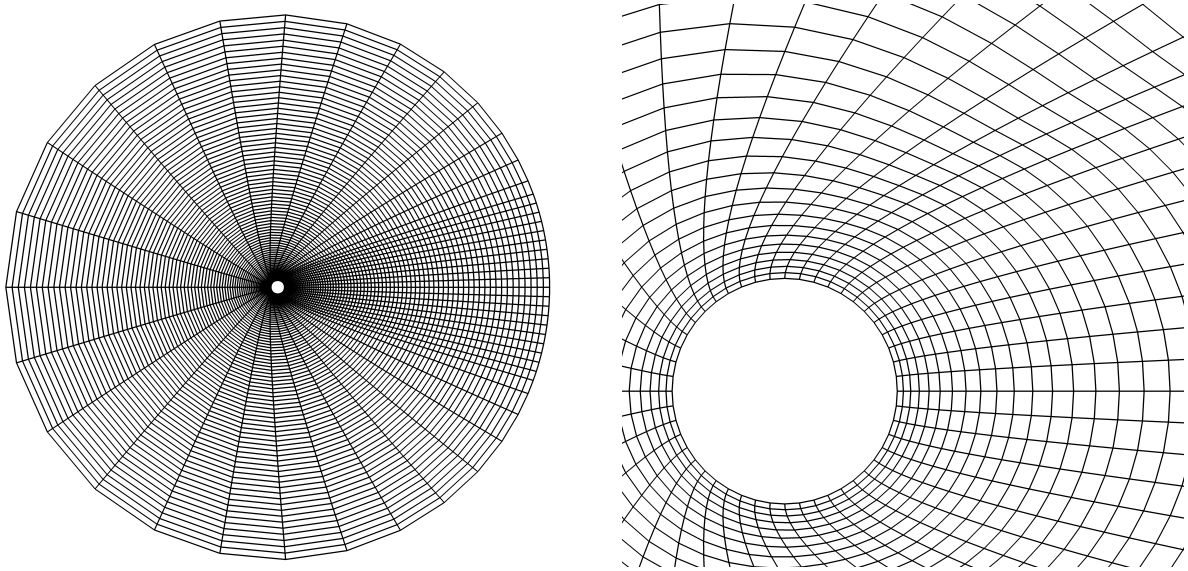

(a) (b)

Figure 3.9: An O-type mesh following the distribution method of Beaudan and Moin [3] is used to resolve the unsteady wake and boundary layer for external flow past a cylinder. It is shown here with all gridlines at the $j = 4$ resolution level.

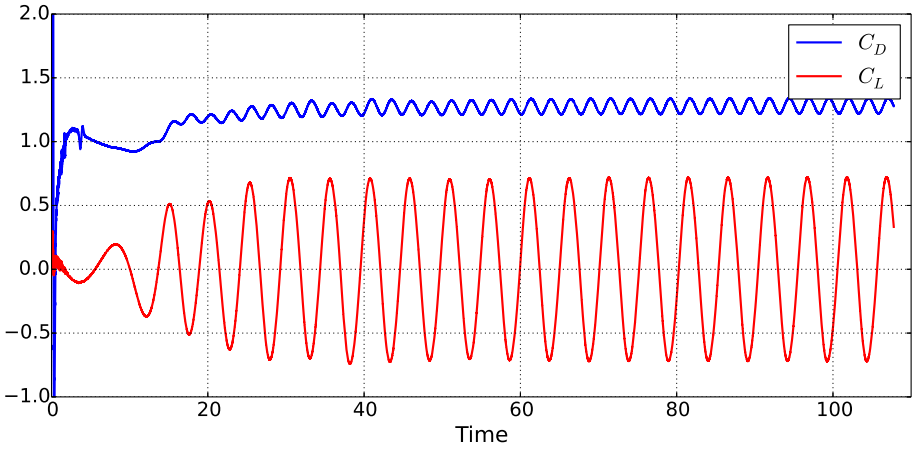

Figure 3.10: Lift and drag forces calculated on the cylinder ($\varepsilon = 10^{-3}$).

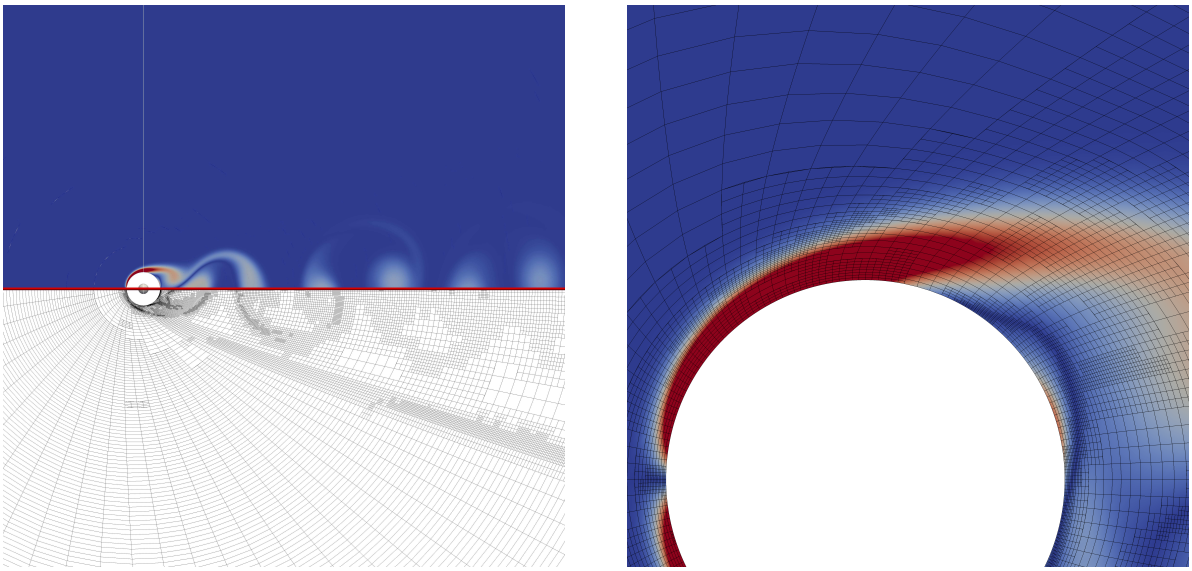

(a) (b)

Figure 3.11: Vorticity field and the adaptive mesh for external flow. Dissipation of vortices in the wake causes decreased grid density farther from the cylinder. To maintain the accuracy of the transform operations, adaptation occurs upon the mesh mappings $\mathbf{x}(\boldsymbol{\xi})$, and is clearly seen in (3.11a).

Chapter 4

Compressible Stochastic Coherent Adaptive Large Eddy Simulation for Bounded Flows

4.1 Introduction

Numerical simulation is an increasingly important component of academic and engineering investigations of turbulent flows. It is a near ubiquitous phenomena in many compressible regimes, including aerodynamics and turbomachinery. Compared to incompressible regimes, the transport flow dynamics are further complicated by varying density and significant thermodynamic changes in these high speed regimes. Though results from direct numerical (DNS) simulation of the Navier-Stokes equations provide tremendous insight, they remain prohibitively expensive for even moderately sized problems due to the vast range of spatial and temporal scales [38] .

Many approaches are used to make the simulations of turbulent regimes tractable, including coarser resolution approximations and dynamic adaptation. In particular, the adaptive wavelet collocation method (AWCM) [70, 76] has been demonstrated as an effective tool, forming a cogent framework for turbulence simulation using a greatly reduced memory footprint [16, 23, 30, 47, 60]. Sharing properties with adaptive mesh refinement (AMR), wavelet-based methods seek to exploit the spatio-temporal intermittency of turbulent vortices by maintaining a sparse data representation, thereby lowering the computational costs through reduced degrees of freedom. A distinguishing advantage is that these approaches provide highly controlled error *a priori* and well behaved, adjustable accuracy. Regions of low variation experience a coarsening of the grid, while steep gradients and highly energetic structures become more well refined.

Stochastic-coherent adaptive large eddy simulation (SCALES) [30] is an approach that combines the tenants of both adaptive wavelet turbulence simulation with the more traditional large eddy simulation (LES), whereby a filtered form of the governing equations is solved upon a reduced, coarser grid. Typically, LES uses a lowpass filter to reduce the computational complexity of the constitutive equations. With sufficient separation between integral and dissipative length scales, the smaller turbulent scales within the inertial sub-range are assumed to take on some universal character [28] whose influence can be deduced from the resolved modes based upon a scaling argument. The retained large scales are presumed to capture the distinctive behavior of particular flow configurations and are directly simulated.

The SCALES method analogously uses an adaptive wavelet filter to construct the LES-like approximation. While lowpass filtering splits the fields into large and small scale flow structures, the wavelet filter decomposes flow into coherent and incoherent components based on a specified filter threshold. The fundamental LES assumption is that, given the scalable cascade of turbulent eddies, the retained modes are sufficient to model the effects of subgrid motions. In the context of traditional LES approximation, this permits lowpass filtering to reduce computational complexity provided separation between large and small scales. By contrast, SCALES discards the stochastic and the least energetic coherent portion of the turbulent solution across all lengthscales. It is thereby assumed that these modes are of a sufficiently universal character to be captured by generalized models. Where this assumption might fail, the effect upon the resolved field is minimized since the wavelet-based subgrid scales represent, by definition, the lowest relative energy content. Taking into account that small-scale coherent structures are largely responsible for subgrid-scale (SGS) stresses in LES [16], many standard LES closures have been successfully applied within the SCALES context, including various eddy viscosity-type approaches [31, 75, 17] and dynamic structure models [17].

While it may seem that SCALES is simply a form of LES that utilizes a different filtering approximation, it should be emphasized that the filtering, gridding, and computational environments are all tightly coupled within the AWCM framework. Simulation occurs on an adaptive grid that automatically refines upon transient, dynamically important flow structures in order to maintain a

consistent discrete approximation. Beyond optimizing the computational complexity, this controls the quality of the mesh and spatial discretization, to which LES results are especially sensitive.

Adaptive wavelet turbulence modeling approaches form a continuously adjustable fidelity hierarchical framework [60]. The highest accuracy is achieved through Wavelet-based Direct Numerical Simulation (WDNS), whereby the full flow field is resolved and the effects of the adaptive wavelet filter are negligible. In this limit, computational costs are reduced only by exploiting spatio-temporal intermittency within the turbulent flow field. At higher levels of wavelet threshold filtering, Coherent Vortex Simulation (CVS) [23, 61, 31], uses the adaptive wavelet filter to de-noise the solution and separate out the purely stochastic modes. The discarded signal, being the Gaussian white noise, has a minimum effect on the evolution of coherent flow structures. It has been found that CVS can adequately recover many statistical quantities of interest by simply discarding these subgrid scale (SGS) motions [16]. In CVS, the kinetic energy from the resolved coherent motions is dissipated through physical viscosity.

Within this wavelet-based simulation hierarchy, SCALES is the lowest fidelity approach as the discarded SGS modes are substantial. In addition to the stochastic/incoherent content that is discarded in CVS, SCALES removes the lowest energy coherent modes. An explicit closure model is therefore necessary since the coherent modes dominate the SGS effects upon the resolved flow field [16]. Furthermore, the complete or partial removal of dissipative length scales necessitates additional mechanisms for the dissipation of turbulent kinetic energy. While SCALES is not predicated on a specific class of LES closure models, certain properties are particularly advantageous for the adaptive wavelet-based simulation framework. For models that automatically switch off in the well resolved and laminar flow regions, control of the overall physical fidelity can be reduced to control of the adaptive wavelet threshold filter [18, 48], thereby forming a fully unified hierarchical modeling framework that transitions continuously between SCALES, CVS, and WDNS. As the filtering parameters are tightened, a greater portion of the velocity field is retained and resolved, lessening the effect of the subgrid scale model, which eventually becomes negligible. The filtering parameters can be adjusted both spatially and temporally based on objective physically-based

criteria throughout the course of the simulation, targeting specific phenomena [18, 48].

Though the wavelet-based turbulence simulation framework has shown to be very promising, its development and study has been relatively limited. Most application has been within the context of incompressible turbulence, and only a few authors have investigated CVS in the low Mach regime of fully compressible transport equations [58]. Furthermore, studies have been limited to a relatively narrow set of configurations, including isotropic turbulence [31, 47], as well as turbulent wake flows behind a bluff body [15, 18]. Though the latter features bounded flows, the Reynolds number was in the transitional regime and the boundary layer itself remained laminar.

Here, SCALES is extended to compressible flows, where variable density and thermodynamic effects arise. The governing equations consist of the wavelet filtered compressible Navier-Stokes equations. Two eddy-viscosity closure models are considered for the resulting filtered nonlinear terms. The first is the Local Dynamic K-Equation Model (LDKM) [12], which is based on the Dynamic Smagorinsky approach [28]. An additional transport equation is solved to track the SGS kinetic energy and locally scale the model terms, which are dynamically determined from the resolved flow field by assuming a scaling relationship between filtering levels. The second approach is the Anisotropic Minimum Dissipation (AMD) approach [59]. This is a simplified method whose computational cost in both memory and complexity are far less than LDKM. Minimum dissipation models seek to approximate the least eddy viscosity necessary to prevent the formation of structures smaller than the grid.

Both of these closures are examined on SCALES simulations of a compressible turbulent channel flow. This configuration also examines the behavior of wavelet-based approaches in cases where boundary layers are fully turbulent. In order to more efficiently resolve all portions of the boundary layer, including to the viscous sublayer, the Adaptive-Anisotropic Wavelet Collocation (A-AWCM) [8] is used, permitting stretching of the wavelet mesh geometry close to the wall.

4.2 Methodology

4.2.1 Adaptive Wavelet Collocation Method

The adaptive wavelet collocation method is a multiresolution approach using a wavelet filter to dynamically adapt a discrete grid to features in the solution. The filter acts by decomposing a discrete scalar field, $u(\mathbf{x})$, into a set of orthogonal or bi-orthogonal wavelet basis functions. Wavelet functions have many attractive properties for multiresolution analysis as they have localized support in both wavenumber and physical space, due to vanishing moments and rapid spatial decay, respectively. In comparison, the Fourier transform provides precise information about the frequency content of a signal, but due to the global support of the Fourier modes, gives no spatial insight.

While there are several classes of wavelets that are suitable for the solution of partial differential equations (PDEs), second generation interpolating wavelets [62] have been implemented here for computational efficiency and their application towards domain partitioning algorithms needed for distributed memory computing [49]. In the wavelet transform, a general field variable is discretized by a series of dyadic, nested grids comprised of collocation points $\mathbf{x}_{\mathbf{k}}^{j}$ on resolution levels j. It can be represented by the series

$$u(\mathbf{x}) = \sum_{l \in \mathcal{L}^0} c_l^0 \phi_l^0(\mathbf{x}) + \sum_{j=1}^{+\infty} \sum_{\mu=1}^{2^n-1} \sum_{\mathbf{k} \in \mathcal{K}} d_{\mathbf{k}}^{\mu,j} \psi_{\mathbf{k}}^{\mu,j}(\mathbf{x}), \tag{4.1}$$

where each basis function corresponds one-to-one with a grid point $k \in \mathcal{K}$. Scaling functions, $\phi_l^0(\mathbf{x})$, carry the averaged signal, while the wavelet functions, $\psi_{\mathbf{k}}^{\mu,j}(\mathbf{x})$, define local, variational details. The amplitudes are given by the coefficients c_l^0 and $d_{\mathbf{k}}^{\mu,j}$, respectively, and likewise have a unique correspondence to grid points. For an arbitrary n-dimensional space, there are $2^n - 1$ families of wavelet functions, μ.

Wavelet threshold filtering arises naturally from the series expansion (4.1). Wavelets whose coefficients fall below some prescribed threshold, ε are discarded. For generality, $\varepsilon = \varepsilon(\mathbf{x}, t)$. The

wavelet-filtered quantity, $\overline{u}^{>\epsilon}(\mathbf{x})$, can be represented as the conditional series

$$\overline{u}^{>\epsilon}(\mathbf{x}) = \sum_{l\in\mathcal{L}^0} c_l^0 \phi_l^0(\mathbf{x}) + \sum_{j=1}^{j_{\max}} \sum_{\mu=1}^{2^n-1} \sum_{\substack{\mathbf{k}\in\mathcal{K} \\ |d_{\mathbf{k}}^{\mu,j}|\geq\varepsilon\|u\|}} d_{\mathbf{k}}^{\mu,j} \psi_{\mathbf{k}}^{\mu,j}(\mathbf{x}), \tag{4.2}$$

whose terms are a subset of (4.1) and consist of the highest energy modes on $j_{\max}$ levels of resolution. In many implementations, the filter threshold is taken to be relative to some characteristic signal amplitude, often either the L_2- or L_∞-norm of $u(\mathbf{x})$ [30], denoted $\|u\|$. The resulting filter operation is nonlinear. For a properly normalized threshold, the reconstruction error of the filtered variable is shown to converge as [21]

$$\|\overline{u}^{>\epsilon} - u\| \leq O(\varepsilon)\,\|u\|\,. \tag{4.3}$$

Dynamic adaptation of the grid is tightly coupled to the wavelet filter, resulting from the localization of wavelet functions in physical space, and their one-to-one correspondence to grid nodes. As modes are filtered, their respective collocation points are omitted from the grid, since the associated value of $\overline{u}^{>\epsilon}(\mathbf{x})$ can be reconstructed (interpolated) using the remaining wavelet functions. The resulting sparse grid exactly reconstructs the filtered field (4.2). It should be noted that the wavelet filter, and therefore wavelet-based interpolation, is not positivity preserving. Since the wavelet modes capture high local energy, the grid is clustered and more refined around strong structures in the flow field, and becomes coarser in regions of low variation.

Adaptation for transient signals is accomplished by predicting collocation points that may become significant in the next time step or iteration, as the wavelet filter only acts to remove points. The sparse grid, supporting $\overline{u}^{>\epsilon}(\mathbf{x})$, is augmented by adding the nearest neighbors to every significant collocation point on the current, next higher, and next lower resolution levels. This reflects a CFL-type argument for the finite-rate transfer of information both spatially and with respect to the wavenumber. Successive application of the wavelet filter and grid augmentation across time effectively tracks and maintains resolution of the structures. For systems that have multiple quantities of interest, each field is filtered separately with independent thresholds and solved on the union of collocation points.. This permits the use of control and proxy variables

to ensure that aspects of the PDE solution are maintained for a prescribed solution fidelity and associated analyses.

As opposed to wavelet Galerkin methods, AWCM seeks to solve PDEs in real space. Derivative approximations are provided by finite-differences at the local adaptive resolution level. Where differencing stencil points do not explicitly exist on the current adaptive wavelet grid, the functional values are interpolated from the underlying wavelet basis functions. A full description of the algorithms can be found in Vasilyev and Bowman [76], Nejadmalayeri et al. [49], and Paolucci et al. [51]. While second generation basis used here requires a *topologically* regular, rectilinear grid, the corresponding explicit *geometric* restriction was recently obviated by use of the Adaptive-Anisotropic Wavelet Collocation Method (A-AWCM) [8]. This extension of AWCM permits curvilinear mesh geometries in order to optimize memory requirements. Within this framework, *a priori* error control described in (4.3) is preserved.

4.2.2 Compressible Stochastic Coherent Adaptive Large Eddy Simulation

Stochastic Coherent Adaptive Large Eddy Simulation leverages both the dynamic adaptivity and the inherent filtering of AWCM. In traditional LES, universal turbulent motions are presumed to be determined solely on the bases of length scale. The transport equations are lowpass filtered and closed using some model for SGS terms. For SCALES, however, the adaptive wavelet grid is used as an implicit grid-level filter, $\overline{(\cdot)}^{>\epsilon}$ that distinguishes between the relative energy content of localized modes. For compressible, variable-density flows, density weighted Favre-filtering is defined with the wavelet thresholding operator as

$$\widetilde{\phi} = \frac{\overline{\rho\phi}^{>\epsilon}}{\overline{\rho}^{>\epsilon}}. \tag{4.4}$$

With the usual assumption of commutation between derivatives and filtering operators, the wavelet Favre-filtered compressible Navier-Stokes equations follow as

$$\frac{\partial \overline{\rho}^{>\epsilon}}{\partial t} = -\frac{\partial}{\partial x_j}\left[\overline{\rho}^{>\epsilon}\widetilde{u}_j\right], \tag{4.5}$$

$$\frac{\partial \overline{\rho}^{>\epsilon}\widetilde{u}_i}{\partial t} = -\frac{\partial}{\partial x_j}\left[\overline{\rho}^{>\epsilon}\widetilde{u}_i\widetilde{u}_j + \overline{p}^{>\epsilon}\delta_{ij} - \widetilde{\sigma}_{ij} + \tau_{ij}\right], \tag{4.6}$$

$$\begin{aligned}\frac{\partial \overline{\rho}^{>\epsilon}\widetilde{e}}{\partial t} = &-\frac{\partial}{\partial x_j}\left[\left(\overline{\rho}^{>\epsilon}\widetilde{e} + \overline{p}^{>\epsilon}\right)\widetilde{u}_j - \widetilde{u}_i\widetilde{\sigma}_{ij}\right. \\ &\left. - \left(\widetilde{\kappa}\frac{\partial \widetilde{T}}{\partial x_j}\right) + C_p q_j\right] + H,\end{aligned} \tag{4.7}$$

where the viscous stress tensor is $\widetilde{\sigma}_{ij} = 2\widetilde{\mu}\widetilde{S}^{\star}_{ij}$ and the traceless strain rate tensor is

$$\widetilde{S^{\star}_{ij}} = \widetilde{S_{ij}} - \frac{1}{3}\widetilde{S_{kk}}\delta_{ij}, \tag{4.8}$$

$$\widetilde{S_{ij}} = \frac{1}{2}\left(\frac{\partial \widetilde{u_i}}{\partial x_j} + \frac{\partial \widetilde{u_j}}{\partial x_i}\right). \tag{4.9}$$

The subgrid scale (SGS) stress and SGS heat flux are given by

$$\tau_{ij} = \overline{\rho}^{>\epsilon}\left(\widetilde{u_i u_j} - \widetilde{u}_i\widetilde{u}_j\right), \tag{4.10}$$

$$q_j = \overline{\rho}^{>\epsilon}\left(\widetilde{Tu_j} - \widetilde{T}\widetilde{u}_j\right), \tag{4.11}$$

respectively. Residual filtered energy terms, H, in (4.7) are

$$H = \frac{\partial}{\partial x_j}\left[\widetilde{\mu}\frac{\partial k}{\partial x_j} + \widetilde{\mu}\frac{\partial}{\partial x_i}\left(\frac{\tau_{ij}}{\overline{\rho}^{>\epsilon}}\right) - f_j\right] - \epsilon_c \tag{4.12}$$

where k, f_j, and ϵ_c are respectively the SGS kinetic energy, triple correlation, and dilatational dissipation, given by

$$k = \frac{1}{2}\tau_{kk}, \tag{4.13}$$

$$f_j = \frac{1}{2}\rho\left(\widetilde{u_i u_i u_j} - \widetilde{u_i u_i}\widetilde{u}_j\right), \tag{4.14}$$

$$\epsilon_c = \frac{\partial}{\partial x_j}\left[\frac{5}{3}\widetilde{\mu}\left(\widetilde{u_j\frac{\partial u_k}{\partial x_k}} - \widetilde{u}_j\widetilde{\frac{\partial u_k}{\partial x_k}}\right)\right]. \tag{4.15}$$

Lastly, the filtered ideal-gas equation

$$\overline{p}^{>\epsilon} = R\overline{\rho}^{>\epsilon}\widetilde{T} \tag{4.16}$$

closes the thermodynamic state of the fluid, where R is the specific gas constant. For the simulations presented here, the specific heats, C_p and C_v, are assumed to be constant.

Specification of the wavelet threshold, $\varepsilon(\mathbf{x}, t)$, rigorously controls the filter and therefore the accuracy of the solution. From this perspective, a wavelet-based hierarchical framework for adjustable fidelity turbulence modeling has emerged from incompressible studies [30, 31, 47]. In the limit $\varepsilon \to 0$, the nonclosed SGS terms τ_{ij}, q_j, k, f_j, and ϵ_c approach zero and the transport equations (4.5-4.7) converge to their non-filtered counterparts. That is, the reconstruction error (4.3) becomes negligible.

Apart from controlling the error, the adaptive wavelet methods act to filter fields based on notion of coherency. At an ideal threshold, the filter separates turbulent fields into purely stochastic and dynamically important structures. With an aggressive ε in SCALES approaches, the lowest energy coherent motions are also discarded and the effect of the SGS terms must be modeled. This includes modeling of energy loss through unresolved viscous effects, and the lowest energies appear at the dissipative length scales in the turbulence cascade. It is proposed with SCALES that the most energetic coherent modes dominate mixing, heat transfer, and other quantities of interest that are characteristic to specific flow configurations. From the opposite perspective, the least energetic modes are considered to be the most universal and permissive of generalized subgrid modeling.

It has been shown by De Stefano et al. [16] that the (low energy) coherent modes in the SGS field dominate the SGS terms. Conversely, by filtering out the most stochastic and least energetic modes, SCALES attempts to minimize the SGS effects that must be modeled. As with all LES approaches, an optimal closure model is an active topic of research within the turbulence community. Favorable modeling approaches for SCALES include those that converge to the non-filtered equations where the flow is laminar or well resolved, as this allows for implementation of a unified wavelet-filtered framework whereby SCALES is able to revert to highly accurate CVS and WDNS where it is needed solely through the control of the AWCM mechanism.

The compressible regime increases the complexity of SCALES, as the chaotic velocity field is influenced by thermodynamic variations and non-constant density. Furthermore, thermodynamic

phenomena commiserate to the turbulent field is often of primary interest for compressible simulations. Inclusion of a thermodynamic transport equation, here the total energy (4.7), increases the number of nonlinear filtered terms that must be modeled. However, many of these, including the SGS heat flux (4.11) are driven by the same mechanism as the SGS stress, namely the subgrid scale velocities, making the extension of SCALES natural to this regime. The use of the ideal gas equation here in lieu of nonlinear real-gas equations of state simplifies the analysis.

With the more complicated physical environment, the options for adaptive markers are greatly increased for compressible flows. A naive implementation would be to adapt on all conserved variables, $\overline{\rho}^{>\epsilon}$, $\overline{\rho}^{>\epsilon}\widetilde{u}_i$, and $\overline{\rho}^{>\epsilon}\widetilde{e}$, though this approach might be sub-optimal for some configurations. Characteristic amplitude scales and particular phenomena of interest are highly problem dependent. For example, aeroacoustic analysis may require accurate resolution of density and pressure linear perturbation fields in order to accurately resolve propagation, whereas drag computations may benefit from the cost savings of approximating these quantities. At minimum, the SCALES framework for high-speed turbulence simulations requires targeted adaptation on the velocity field and resolution of any velocity driving thermodynamic effects.

While the computational framework is similar, a distinction should be made between SCALES and adaptive LES using a lowpass filter. In the latter, a lowpass filter is imposed by limiting the maximum resolution in (4.2). This approach is consistent with traditional LES as the filtering is prescribed at some length scale within the inertial range of the turbulent energy cascade. A very low wavelet threshold, ε, is imposed, ensuring that the residual of the *wavelet* filter is minimal and the transport equations approach the *lowpass* filtered equivalent. Reduction in memory footprint from the wavelet-based adaptation would then be entirely realized through intermittency at these larger length scales.

4.2.3 Closure Models

As the coherent part of the SGS turbulent quantities dominate the effect on the resolved field, standard closure models are presumed to capture these coherent modes [16] in a similar fashion as in

incompressible SCALES. Two compressible SGS turbulence models are examined here, namely the LDKM approach of Chai and Mahesh [12] and the reduced cost AMD model proposed by Rozema et al. [59]. These are both eddy-viscosity approaches, whereby the effects of the SGS modes are considered to behave as dissipative forces that can be deduced from larger scales. Both provide a localized, dynamic estimation of SGS effects that take full advantage of the adaptivity of SCALES for complex turbulent flows without geometric averaging. Furthermore, they exhibit attractive convergence properties, whereby the modeled terms are implicitly coupled to ε by automatically reducing to zero in well resolved or laminar regions.

4.2.3.1 Local Dynamic K-Equation Model

The LDKM class of approaches were first proposed by Ghosal et al. [29] as a variation on the dynamic Smagorinsky model that explicitly tracks a budget of the SGS kinetic energy (4.13), enabling localized computation of SGS terms while maintaining stability. Incompressible forms of LDKM have been successfully implemented in a SCALES context [17] for several flow configurations.

For compressible flows, a version was developed by Chai and Mahesh [12]. The wavelet Favre-filtered transport equation for the SGS kinetic energy, k, is given by

$$\begin{aligned}\frac{\partial \overline{\rho}^{>\epsilon} k}{\partial t} = &- \frac{\partial}{\partial x_j}\left[\overline{\rho}^{>\epsilon} k \widetilde{u_j} - \tau_{ij}\widetilde{u_i} - \widetilde{\mu}\frac{\partial k}{\partial x_j}\right. \\ &\left. -\widetilde{\mu}\frac{\partial}{\partial x_i}\left(\frac{\tau_{ij}}{\overline{\rho}^{>\epsilon}}\right) - Rq_j\right] \\ &- \tau_{ij}\widetilde{S_{ij}} - \epsilon_s - \epsilon_c - \frac{\partial f}{\partial x_j} + \Pi\end{aligned} \tag{4.17}$$

where the solonoidal dissipation, ϵ_s, and pressure–dilatation, Π, are

$$\epsilon_s = 2\widetilde{\mu}\left[\widetilde{S^\star_{ij} D^\star_{ij}} - \widetilde{S^\star_{ij}}\,\widetilde{D^\star_{ij}}\right], \tag{4.18}$$

$$\Pi = \overline{p\frac{\partial u_k}{\partial x_k}}^{>\epsilon} - \overline{p}^{>\epsilon}\widetilde{\frac{\partial u_k}{\partial x_k}}, \tag{4.19}$$

and $\widetilde{D^\star_{ij}}$ is the traceless velocity gradient tensor.

To model the nonlinear filtered terms in the transport equations, (4.5-4.7) and (4.17), the

following models are used:

$$\tau_{ij} - \frac{1}{3}\tau_{kk}\delta_{ij} = -2C_s\Delta\overline{\rho}^{>\epsilon}\sqrt{k}\widetilde{S^{\star}_{ij}}, \tag{4.20}$$

$$q_j = -\frac{C_s\Delta\overline{\rho}^{>\epsilon}\sqrt{k}}{\mathrm{Pr}_T}\frac{\partial\widetilde{T}}{\partial x_j}, \tag{4.21}$$

$$f_j = C_f\Delta\overline{\rho}^{>\epsilon}\sqrt{k}\frac{\partial k}{\partial x_j}, \tag{4.22}$$

$$\epsilon_c = \frac{C_{\epsilon c}M_T^2\overline{\rho}^{>\epsilon}k^{3/2}}{\Delta}, \tag{4.23}$$

$$\epsilon_s = \frac{C_{\epsilon s}\overline{\rho}^{>\epsilon}k^{3/2}}{\Delta}, \tag{4.24}$$

where C_s, C_f, $C_{\epsilon c}$, and $C_{\epsilon s}$ are closure coefficients, Pr_T is the turbulent Prandtl number, Δ is the nominal local filter width (as a function of the local resolution level), and $M_t = \sqrt{2k}/a_0$ is the turbulent Mach number based on the subgrid scale modes. As noted by Chai and Mahesh [12], the pressure dilatation term, Π, can be neglected to reduce computational costs and still recover satisfactory statistical results.

The model coefficients in (4.20-4.24) are determined through the dynamic procedure [39]. By test-filtering the resolved SCALES field and assuming some scale similarity or analogy relationship, the coefficients can be deterministically computed. This particular implementation of LDKM follows that of Chai and Mahesh [12], where C_s, C_f, and Pr_T are computed using Germano-like scaling [44, 39], and the dissipation coefficients $C_{\epsilon c}$, and $C_{\epsilon s}$ use the scaling law of Menon and Kim [42]. A local lowpass filter is used for the test-level filter in the dynamic procedure.

One of the prime advantages of LDKM is that it permits negative values for C_s, emulating a return of kinetic energy to the resolved scales. The inherent instability of the resulting negative dissipation terms is limited by the budget of local SGS kinetic energy, $k(\mathbf{x})$, through the production term $-\tau_{ij}\widetilde{S_{ij}}$.

4.2.3.2 Anisotropic Minimum Dissipation

Minimum dissiaption models are less costly alternatives that feature both dynamic computation and well behaved convergence properties. They are a recent family of closure models, the

earliest being the QR model [77, 78], designed to estimate the minimum amount of eddy-dissipation required to remove the subgrid scales from the LES solution. They use Poincaré's inequality to bound a dissipation term that prevents the accumulation of energy at scales the are smaller than the local LES filter width, Δ. Rather than relying on similarity arguments and a universal behavior of turbulent energies across lengthscales, minimum dissipation approaches seek to minimize the effect of the eddy-viscosity model assumption. As the algorithm does not require test-level filtering, spatio-temporal averaging, or additional transport equations, it can have inherent cost benefits over models involving the dynamic procedure, such as the well known approach of Germano et al. [28].

The Anisotropic Minimum Dissipation (AMD) model [59] addresses a deficiency in the original QR approach when applied to anisotropic grids. The LES results were shown to be highly sensitive to the filter width approximation Δ. While the geometric mean of each filter direction is conventionally used, $\Delta = (\Delta_x \Delta_y \Delta_z)^{1/3}$, no general approximation for Δ was shown to be widely robust. Alternatively, the AMD eddy viscosity, ν_e, is derived by modifying the Poincaré inequality to explicitly account for grid anisotropy, yielding

$$\nu_e = C \frac{\max\left(-\Delta_k \dfrac{\partial \widetilde{u}_i}{\partial x_k} \Delta_l \dfrac{\partial \widetilde{u}_j}{\partial x_l} \widetilde{S_{ij}}, 0\right)}{\dfrac{\partial \widetilde{u}_m}{\partial x_n} \dfrac{\partial \widetilde{u}_m}{\partial x_n}}, \tag{4.25}$$

where the constant C is determined by the derivative operator. For the central fourth-order finite differences used in this paper, $C = 0.212$ is used in accordance with the original formulation [59].

For generalization to complex mesh geometries, compressible SCALES is implemented here using the Adaptive-Anisotropic Wavelet Collocation Method (A-AWCM) [8]. A spatial transform is used in A-AWCM to admit curvilinear meshes while retaining the rectilinear grid necessary to support the wavelet filter. The computational grid is defined in the curvilinear coordinates, $\xi(\mathbf{x})$. In this context, (4.25) can be directly adapted for the transformed coordinate systems in terms of the computational space grid spacing, $\mathbf{\Delta}_\mathbf{i}^\xi = \left\{\Delta_1^\xi, \Delta_2^\xi, \Delta_3^\xi\right\}$, which is readily available. The eddy

viscosity is therefore computed as

$$\nu_e = C \frac{\max\left(-\Delta_k^\xi \frac{\partial \widetilde{u}_i}{\partial \xi_k} \Delta_l^\xi \frac{\partial \widetilde{u}_j}{\partial \xi_l} \widetilde{S_{ij}}, 0\right)}{\frac{\partial \widetilde{u}_m}{\partial x_n} \frac{\partial \widetilde{u}_m}{\partial x_n}}. \tag{4.26}$$

Note that in numerator of the right hand side of 4.26, both the grid-level filter sizes and spatial derivatives are given in computational space, while velocity and strain rate components are still defined in physical space with respect to $\mathbf{x}$. The dominant SGS terms are then modeled as

$$\tau_{ij} = -2\mu_t \widetilde{S_{ij}^\star}, \tag{4.27}$$

$$q_j = \frac{\mu_t}{\mathrm{Pr}_T} \frac{\partial \widetilde{T}}{\partial x_j}, \tag{4.28}$$

where $\mu_t = \overline{\rho}^{>\epsilon} \nu_e$ and the turbulent Prandtl number is a constant. Residual terms in (4.5-4.7) have been neglected.

In this form, (4.26) does not admit backscatter effects and is limited to positive values of ν_e. Simplified closure models for SCALES are justified by their lower computational cost and the controllable fidelity of the wavelet-based turbulence modeling framework.

4.3 Turbulent Channel Flow

To validate the extension of SCALES to compressible flows, simulations of high-speed channel turbulence have been performed. This configuration examines the application of the method for fully turbulent boundary layers, a context hereto unexplored with AWCM turbulence methods. Fourth order wavelets and finite differences are used to compute both the Navier-Stokes and closure terms, and a lowpass box filter with a width of the local grid spacing provides the test-level filtering for the LDKM model.

The channel flow configuration follows the DNS benchmarks of Morinishi et al. [45] and Foysi et al. [26]. Isothermal walls are imposed on the boundaries normal to the y-axis, and the domain is periodic in the streamwise (x) and spanwise (z) directions. Constant mass flux is maintained by a body forcing term applied in the streamwise direction. Scaled by the channel half-width, H,

the domain measures $L = [4\pi H \times 2H \times 4\pi H/3]$. The bulk Reynolds number is $\mathrm{Re} = \rho_m u_m H/\mu_w$, and the Mach number is $\mathrm{Ma} = u_m/c_w$, where $(\cdot)_m$ denotes bulk mean quantities and c is the speed of sound. Reynolds averaging is indicated by $\langle\cdot\rangle$, with $(\cdot)_w$ signifying quantities averaged at the walls. Density weighted (Favre) averages are noted by $\{\cdot\}$. The friction Reynolds number is given by $\mathrm{Re}_\tau = H/\delta_\nu$, where $\delta_\nu = \mu_w/(\rho_w u_\tau)$ and the friction velocity $u_\tau = (\tau_w/\rho_w)^{1/2}$. Here, τ_w indicates the resolved wall shear stress. Two configurations are considered here: $\mathrm{Re} = 3000$ and $\mathrm{Re} = 6000$, and corresponding Mach numbers of $\mathrm{Ma} = 1.5$ and $\mathrm{Ma} = 3$. Both cases use a Prandtl number of $\mathrm{Pr} = 0.72$ and adiabatic index of $\gamma = 1.4$. As the high Mach numbers introduce large thermodynamic variations, temperature dependent viscosity is given by Sutherland's law, normalized as

$$\frac{\mu}{\mu_w} = \frac{1 + S_1/T_w}{T/T_w + S_1/T_w}\left(\frac{T}{T_w}\right)^{3/2}, \tag{4.29}$$

with the constant $S_1/T_w = 0.3765$.

Simulations at both Reynolds numbers use the same base grid of $M = [20 \times 7 \times 10]$, with adaptive parameters as shown in Table 4.1. For all cases, much higher spatial resolution was permitted than in the reference DNS, though a lower order derivative approximation is used here. A notable difference is that a much lower aspect ratio was used in the present SCALES simulations, as it was found to retain far fewer adaptive grid points. Using A-AWCM, the mesh is stretched in the wall normal direction according to a hyperbolic tangent distribution with the first point located at $\Delta x^+ \approx 0.145$. The maximum adaptable grid refinement is therefore sufficient to support DNS and resolve the dissipative lengthscales in the flow, thus making ensuring that the effect of the cutoff refinement level is minimal. Aggressive wavelet thresholding of $\varepsilon = 10^{-1}$ is applied. The momenta, total energy, and temperature fields are used as the sensors for the adaptive wavelet filter in order to capture both kinematic and thermodynamic phenomena.

The simulations are initialized with a parabolic mean velocity profile, $\overline{u}^{>\epsilon}$, and a constant density and temperature. For optimal perturbation [10], the least stable eigenfunctions were superimposed upon the initial velocity to hasten the transition to fully developed turbulence. A

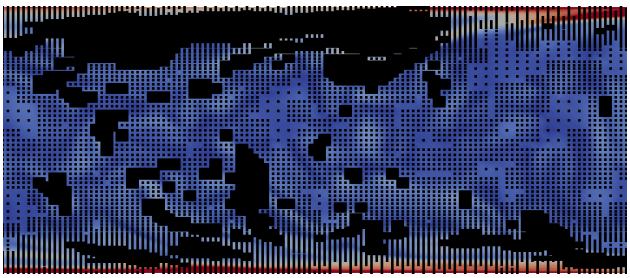

Figure 4.1: The adaptive grid on a section of the turbulent vorticity field within the channel.

low initial wavelet threshold, $\varepsilon_0 = 10^{-2}$ was used for the first several flow through times, limiting the damping effects of the wavelet filter on low amplitude instabilities, permitting them to grow through transition to fully developed turbulence. As the early time solution is relatively smooth, the increased computational cost was mitigated.

The adaptive grid for the developed turbulent flow field is illustrated in Figure 4.1, demonstrating refinement around localized structures. The compression ratio $\mathcal{R}$, defined as the percentage of collocation points retained by the grid, is of a similar order of magnitude to that found in incompressible SCALES studies of homogeneous isotropic turbulence [46, 47]. The higher Re cases correspond with a notable increase in grid compression, retaining a lower fraction of the total points. Further studies will be required to fully characterize the Reynolds number scaling for high speed channel flows.

The results of the SCALES simulations compare well with the benchmark DNS solutions [26, 45]. Statistics were computed from the adaptive grid by interpolating the continuous wavelet basis onto regular, nonadaptive sampling grids. As a reference, the friction Reynolds numbers

Case	Re	Model	$[N_x \times N_y \times N_z]_{\max}$	$j_{\max}$	$\mathcal{R}$	Re_τ
1	3000	AMD	$1280 \times 448 \times 640$	7	0.95%	205
2	3000	LDKM	$1280 \times 448 \times 640$	7	1.01%	207
3	6000	AMD	$2560 \times 896 \times 1280$	8	0.24%	505
4	6000	LDKM	$2560 \times 896 \times 1280$	8	0.29%	512

Table 4.1: Computational and flow parameters. The maximum resolution is dictated by the highest refinement level, $j_{\max}$. The adaptive compression ratio $\mathcal{R}$is the percentage of total grid points that were retained in the simulation.

found in the DNS are $\mathrm{Re}_\tau = 221$ and 556 for the $\mathrm{Re} = 3000$ and 6000 cases, respectively [26]. For all of the SCALES simulations presented here, the the average wall shear stress is under predicted by $O(10\%)$. This discrepancy corresponds with the order of error introduced by the high adaptive wavelet threshold of $\varepsilon = 10^{-1}$. The use of an aggressive threshold in SCALES simulations is justified by the ability to reconstruct *statistical* quantities in spite of the elevated error in the deterministic solution. In the near-wall region, where the structure of the flow is not truly turbulent, the global SCALES approximation is inconsistent with capturing the functional shape of the viscous sub-layer to a high degree of accuracy.

In spite of this difference, turbulent statistics compare well with the DNS data across the closure models and Reynolds numbers considered here. Velocity statistics are shown in Figure 4.2, where Favre fluctuations are indicated by $(\cdot)''$ and Reynolds fluctuations are denoted $(\cdot)'$. The streamwise 4.2a and spanwise 4.2b Reynolds stresses have good general agreement with the benchmark results, predicting the location of maximum stress near the wall. The magnitudes of the profiles computed from the SCALES simulations are slightly lower than found in the DNS data for $y^+ > 20$, as the energy content of the discarded wavelet modes is non-negligible.

Mach number effects manifest, in part, as heating from the dissipation of kinetic energy. With isothermal boundaries, this results in elevated temperatures within the channel and increased density at the walls as fluid mass has been displaced. The average density profiles are shown in Figure 4.2c with increased gradients and density variation corresponding with the increased Mach number.

The Van Driest transformation of the average streamwise velocity, shown in Figure 4.2d, is

$$\langle u_1 \rangle^+_{VD} = \int_0^{u_1^+} \left(\langle \rho \rangle / \rho_w \right)^{1/2} d\langle u_1 \rangle. \tag{4.30}$$

It is clearly seen that the SCALES simulations not only capture the universal log-law profile, but also manifest the slight Re-associated discrepancies found in the DNS benchmarks [26]. A subtle underprediction of $\langle u_1 \rangle^+_{VD}$ near the wall coincides with the depressed wall shear stress, τ_w, while the higher values at $y^+ > 20$ are reflected in the higher average density in the same region.

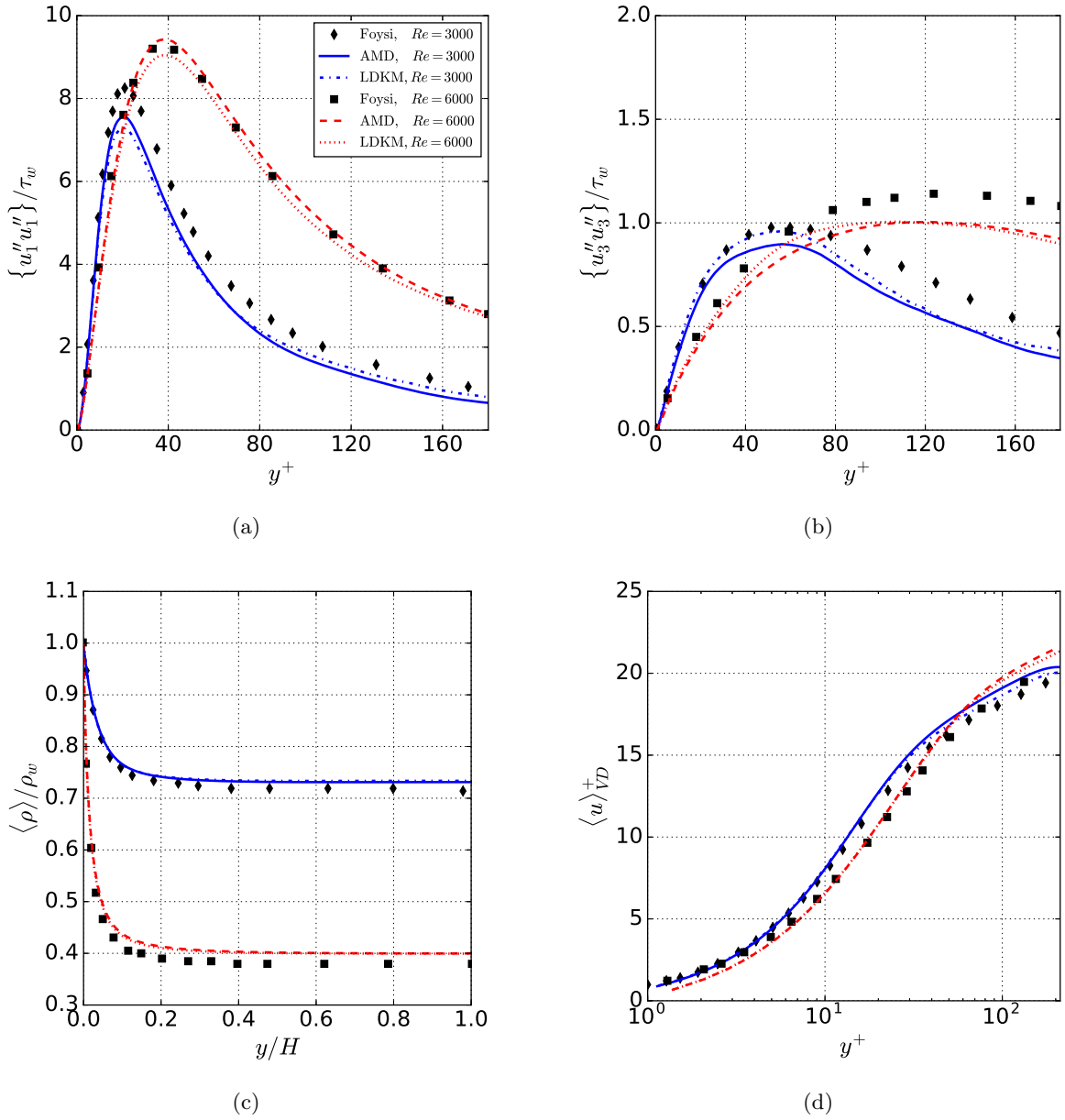

Figure 4.2: Profiles of the Reynolds stresses in the streamwise (a) and spanwise (b) directions, the averaged density (c) and Van Driest-transformed mean velocity (d). Profiles are compared to the DNS results of Foysi et al. [26].

One of the primary purposes of this investigation is to ascertain the ability of the SCALES approach to adequately capture compressibility effects and the corresponding fluctuations in the thermodynamic quantities. The RMS of the fluctuating density, ρ'_{rms}/ρ_w, and temperature, T'_{rms}/T_w, are shown in Figure 4.3, with comparative DNS data available only for Re = 3000. The results align well with the benchmark case. The Re = 6000 flow configuration shows a similar profile with the peak fluctuation RMS located very close to the boundary. The increase in Mach number manifests as increased thermodynamic variation throughout the width of the channel.

The high accuracy of the density perturbations near and on the wall highlight two points of note for the SCALES approach. First, the increase in accuracy near the wall for all statistics shown here largely arises from the increase in adaptive resolution. High gradients in velocity and temperature in the inner boundary layer cause increased local adaptation in the collocation grid. In contrast, adaptation in the center of the domain is a result only of the fluctuating quantities upon a low-gradient mean flow. The disparate flow conditions result in different resolution of the *turbulent* phenomena throughout the domain. Second, the improvement in the accuracy of computed turbulent statistics coincides with the same region where the normal shear stress, τ_w, manifests a large error. This reinforces the idea that the SCALES methodology differs in its ability to predict statistical versus deterministic quantities. The straightforward global application of SCALES to turbulent channel flows, which contain quantities of interest of both types, is more amenable to the former.

The accuracy of both the LDKM and AMD closure models was found to be similar across both flow configurations considered here. Differences between the results computed with each model are minimal and dependent upon the quantity examined. The average point count, as noted in Table 4.1 by the active point ratio $\mathcal{R}$, was higher for LDKM, though generally comparable.

The slightly higher point count of the LDKM simulations may be coupled to the lower RMS eddy viscosity, μ_T, illustrated in Figure 4.4. Additionally, LDKM admits backscatter-type effects through negative diffusion which is inherently unstable. Both of these effects can contribute to the retention of energy in high wavenumbers and commensurately increased resolution. Indeed, one of

the principle stabilizing mechanisms for negative eddy viscosity within the SCALES framework is the ability to adapt upon unstable regions. Increasing resolution deactivates the modeled terms (4.20-4.24) via the dynamic test filtering procedure.

The $\mu_{T,rms}$ profiles confirm that both models automatically converge to zero at the wall without the need of additional damping functions. The LDKM model is more localized to the turbulence-producing region within the boundary layer and the RMS profile rapidly reducing in the center of the channel. In contrast, the AMD closure maintains a more consistent level throughout the full domain. Increased eddy viscosity is seen throughout the domain for the higher Reynolds number flows.

The similarity of results between the LDKM and AMD models is notable. Much of the motivation behind more sophisticated LES closures is to better predict generalized turbulent flows, that is non-homogeneous and anisotropic configurations, with lower computational cost. However, the numerical landscape of wavelet based methods is distinct from traditional LES, as it implements a wavelet rather than a lowpass filter. Indeed, the maximum resolution for these SCALES simulations is comparable to DNS. The adaptive wavelet filter, by discarding low energy modes, acts as an *implicit* component to the LES model. Within this framework, the current results indicate that the choice of the *explicit* closure have a mitigated impact for the flow configurations considered. For example, the LDKM closure separately considers and dynamically computes the SGS heat flux 4.21, but predicts ρ'_{rms} and T'_{rms} profiles that are essentially indistinguishable from the AMD closure, which relies on a simplified constant Pr_T assumption.

With this result, AMD is advantageous with a minimal computational cost. The closure term (4.26) involves only algebraic reductions of the velocity gradient tensor, and is trivially extendable to curvilinear meshes. In contrast, the LDKM closure requires application of the dynamic procedure across five terms: (4.20-4.24). Each computation of the dynamic procedure involves multiple lowpass, test level filtering operations. Furthermore, LDKM involves the solution of an additional transport equation. It should be noted, however, that it remains an open question whether this accuracy parity can be expected for other configurations, such as shock/turbulence interaction,

supercritical pressure flows or combusting regimes.

4.4 Conclusions

The SCALES method for wavelet-based turbulence modeling has been extended to the compressible regime, and examined for fully turbulent boundary layers. Simulations were performed for multiple compressible channel flow configurations, implementing LDKM and AMD approaches to close nonlinear terms arising from filtering the transport equations.

While the average wall shear stress was underpredicted due to the aggressive wavelet threshold filter, the computed turbulent statistics were well matched with established DNS results. Of particular note for the high speed regime, thermodynamic quantities were reasonably captured through the SCALES approach. The channel flow configuration poses a hereto unexplored regime for wavelet based methods, as fully developed turbulent features rapidly transition to the laminar structure of the viscous sub-layer. Development of automated approaches for simultaneously capturing these deterministic structures at high accuracy while providing a low cost approach to turbulence modeling is a topic of ongoing research.

Of the explicit models examined here, the implementation had a muted effect on the resolved solution. Both the AMD and LDKM closures are dynamic eddy viscosity models with favorable convergence properties where the forcing terms vanish for well resolved, laminar, and boundary regions. While the LDKM closure model is much more sophisticated, tracking SGS energy budgets and emulating backscatter effects, the simpler AMD model produced results of similar quality within the SCALES framework. This is an important result for the extension of SCALES into applied contexts where the cost savings of simple closure models becomes important.

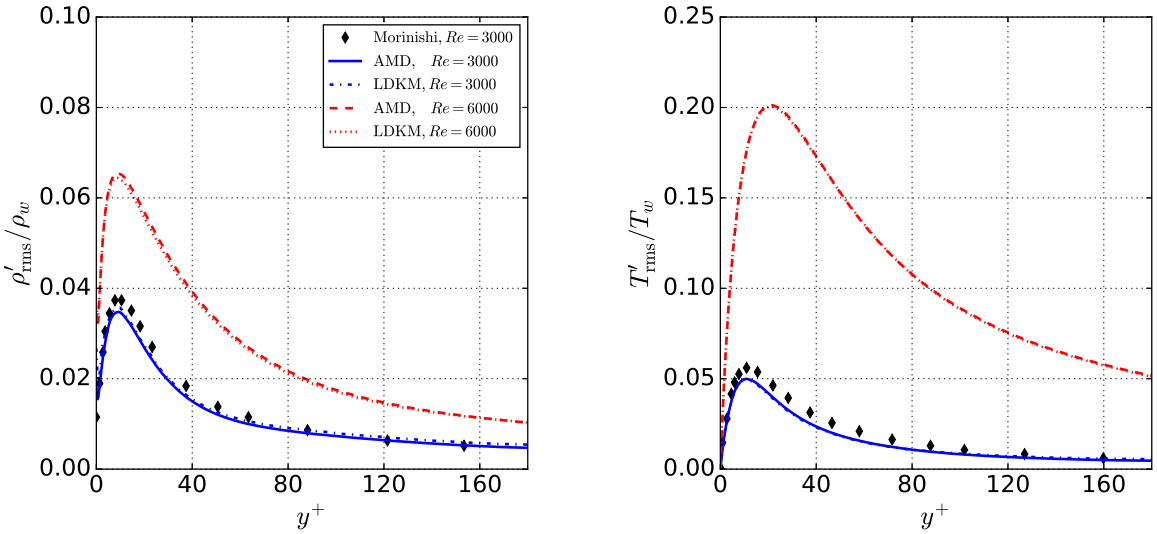

(a) (b)

Figure 4.3: Profiles for the Reynolds fluctuation RMS of density (a) and temperature (b) compared to the DNS results of Morinishi et al. [45] for the case of Re = 3000. Comparative results were not available for these quantities at Re = 6000.

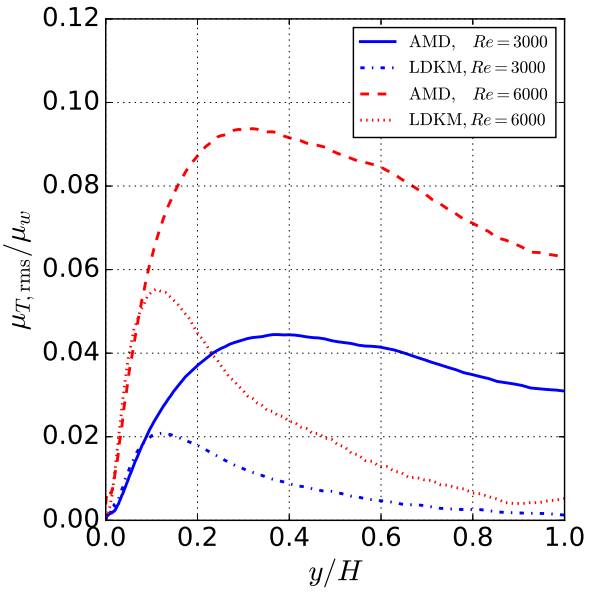

Figure 4.4: The RMS of the eddy viscosity for both closure models, scaled by the molecular viscosity at the wall. Note that the LDKM approach admits locally negative values for μ_T.

Chapter 5

Conclusion and Future Research

5.1 Conclusions

Application of wavelet-based LES methods to high speed flows and configurations of engineering interest requires the extension of SCALES techniques to the compressible regime and the development of approaches to efficiently capture complex geometries. A series of methodologies has been proposed to address these deficiencies and provide a framework for efficient turbulent simulation in this regime.

The generalized boundary condition approach of CBVP and the flexibility of A-AWCM form powerful tools for introducing complex geometries into the otherwise restrictive wavelet environment. Furthermore, the ability to provide localized anisotropic mesh geometry greatly mitigates one of the major shortcomings of AWCM: the so-called curse of isotropy. Isotropic grid refinement incurs prohibitively high expense in the presence of sheet- and filament-like structures. Given the prevalence of wall-bounded flows in engineering applications, this restriction had previously precluded the use of AWCM as a practical tool. The development of A-AWCM has been shown to permit highly efficient sparse data representations in these otherwise untenable configurations. Importantly, A-AWCM preserves the rigorous accuracy control of multiresolution wavelet analysis independent of the underlying mesh geometry. In this way, it addresses one of the principle difficulties of static curvilinear meshes; namely, it guarantees that the grid is sufficiently well resolved to maintain the desired discrete approximation of field variables.

A priori fidelity control and coherency filtering form the basis of the wavelet turbulence

modeling framework, which has been extended here to the compressible regime and examined for the first time on cases involving fully turbulent boundary layers. In addition to the filtered momentum equation, the wavelet filtered continuity and energy-transport equations are modeled and solved. Sensor variables for the adaptive grid were chosen so that both kinematic and thermodynamic phenomena would be resolved at the desired level. Two separate closure models have been demonstrated successfully for high-speed channel flow. For the case considered, the solution quality of the low cost AMD model was on par with the more expensive LDKM closure, which explicitly tracks an estimate of the SGS kinetic energy budget. The use of low cost models increases the attractiveness and applicability of SCALES for applied engineering analysis where total simulation cost is a crucial factor.

5.2 Future Research

Further development efforts are ongoing for advanced curvilinear meshing methods that exploit the particular A-AWCM environment. As the wavelet refinement maintains the accuracy of the solution in a compressed form, there is a large degree of flexibility inherent for specifying the mesh geometry. An un-optimally distributed mesh will not detrimentally impact the solution quality, provided that the mesh is well conditioned for the coordinate transform. Aggressive meshing procedures can therefore be employed biased heavily towards capturing anisotropic structures and mapping to boundaries. Meshing metrics target regions and structures of highly orientable anisotropy in order to ultimately provide a more efficient sparse data representation through AWCM.

There is ongoing work in development of dynamic mesh redistribution algorithms, in which a meshing equation is solved in a time-accurate manner and coupled to the physical transport PDEs. Statistical quantities in the flow solution, such as averaged boundary layers, are then used to inform the mesh. The purpose is to provide optimal sparse data representations without *a priori* knowledge of the flow. One of the difficulties of mesh redistribution for transient flows has been the danger of losing discrete approximation of the underlying fields during the redistribution process.

A-AWCM obviates this failure mode, as it guarantees that the signal is retained at the desired accuracy by adding grid point density in the required regions.

The application of SCALES for fully resolved boundary layers manifests the limitations of the method, namely its applicability modeling only the purely turbulent component of the flow. In this sense, SCALES is not a complete method for simulation of complex flows that involve both distinctly turbulent and laminar qualities. Proposed solutions have involved dynamic feedback loops that locally specify the wavelet threshold, $\varepsilon(\mathbf{x}, t)$, in time and space [48, 18]. While these solutions for a unified engineering simulation framework are promising, their application has been limited to flows that are well partitioned between laminar (boundary layers) and turbulent regions (bluff body wakes). It remains an open question whether these approaches are well suited or optimal for fully developed boundary layers where the turbulent and laminar qualities transition in close proximity in the inner layer.

An alternative approach is proposed that is more consistent with the underlying philosophy of SCALES modeling. The flow field is decomposed into the average $\langle u \rangle$ and perturbation u' quantities in situ on the sparse, adaptive grid. By resolving the averaged field $\langle u \rangle$ to a high accuracy, that is $\varepsilon < 10^{-3}$, it is hypothesized that the laminar features, such as the viscous sub-layer, will be accurately captured. It is then philosophically consistent to apply the SCALES approach to the turbulent fluctuating quantities. Examination of such variable thresholding approaches is an ongoing effort.

Lastly, the methods presented here enable new opportunities for efficient turbulence simulation in thermodynamically interesting regimes. Future efforts are directed towards application of these methods for numerical experiments and investigations into problems of engineering and academic interest that have been hereto untenable.

Bibliography

[1] P. Angot, C.-H. Bruneau, and P. Fabrie. A penalization method to take into account obstacles in viscous flows. Numerische Mathematik, 81:497–520, 1999.

[2] Youngmin Bae and Young J. Moon. On the use of brinkman penalization method for computation of acoustic scattering from complex boundaries. Computers & Fluids, 55(0):48–56, 2012. ISSN 0045-7930.

[3] Patrick Beaudan and Parviz Moin. Numerical experiments on the flow past a circular cylinder at sub-critical reynolds number. Technical report, DTIC Document, 1994.

[4] Hugh M Blackburn and Ron D Henderson. A study of two-dimensional flow past an oscillating cylinder. Journal of Fluid Mechanics, 385:255–286, 1999.

[5] O. Boiron, G. Chiavassa, and R. Donat. A high-resolution penalization method for large mach number flows in the presence of obstacles. Computers and Fluids, 38:703–714, 2009.

[6] K. S. Brentner, J. S. Cox, C. L. Rumsey, and B. A. Younis. Computation of sound generated by flow over a circular cylinder: an acoustic analogy approach. In C. K. W. Tam and J. C. Hardin, editors, Second Computational Aeroacoustics (CAA) Workshop on Benchmark Problems, pages 289–295. NASA, June 1997.

[7] Eric Brown-Dymkoski and Oleg V. Vasilyev. Compressible stochastic coherent adaptive large eddy simulation of wall-bounded flows. in prep.

[8] Eric Brown-Dymkoski and Oleg V. Vasilyev. Adaptive-anisotropic wavelet collocation method on general curvilinear coordinate systems. Journal of Computational Physics, under review.

[9] Eric Brown-Dymkoski, Nurlybek Kasimov, and Oleg V. Vasilyev. A characteristic based volume penalization method for general evolution problems applied to compressible viscous flows. Journal of Computational Physics, 262(2):344–357, 2015.

[10] Kathryn M Butler and Brian F Farrell. Three-dimensional optimal perturbations in viscous shear flow. Physics of Fluids A: Fluid Dynamics, 4(8):1637–1650, 1992.

[11] John Rozier Cannon. The One-Dimensional Heat Equation. Addison-Wesley, 1984.

[12] Xiaochuan Chai and Krishnan Mahesh. Dynamic-equation model for large-eddy simulation of compressible flows. Journal of Fluid Mechanics, 699:385–413, 2012.

[13] Albert Cohen. Adaptive methods for pde's wavelets or mesh refinement? In Proceedings of the ICM, volume 1, pages 607–620. arXiv:math/0212414, 2002.

[14] M. Coutanceau and R. Bouard. Experimental determination of the main features of viscous flow in the wake of a circular cylinder in uniform translation. part 1. steady flow. Journal ofFluid Mechanics, 79:231–256, 1977.

[15] Giuliano De Stefano and Oleg V Vasilyev. Wavelet-based adaptive simulations of three-dimensional flow past a square cylinder. Journal of Fluid Mechanics, 748:433–456, 2014.

[16] Giuliano De Stefano, Daniel E Goldstein, and Oleg V Vasilyev. On the role of subgrid-scale coherent modes in large-eddy simulation. Journal of Fluid Mechanics, 525:263–274, 2005.

[17] Giuliano De Stefano, Oleg V Vasilyev, and Daniel E Goldstein. Localized dynamic kinetic-energy-based models for stochastic coherent adaptive large eddy simulation. Physics of Fluids, 20(4):045102, 2008.

[18] Giuliano De Stefano, Alireza Nejadmalayeri, and Oleg V Vasilyev. Wall-resolved wavelet-based adaptive large-eddy simulation of bluff-body flows with variable thresholding. Journal of Fluid Mechanics, 788:303–336, 2016.

[19] M. D. de Tullio, P. De Palma, G. Iaccarino, G. Pascazio, and M. Napolitano. An immersed boundary method for compressible flows using local grid refinement. Journal of Computational Physics, 225:2098–2117, 2007.

[20] S. C. R. Dennis and Gau-Zu Chang. Numerical solutions for steady flow past a circular cylinder at Reynolds numbers up to 100. Journal of Fluid Mechanics, 42:471–489, 1970.

[21] David L Donoho. Interpolating wavelet transforms. Technical report, Department of Statistics, Stanford University, October 1992.

[22] A S Dvinsky. Adaptive grid generation from harmonic maps on riemannian-manifolds. J. Comp. Phys., 95(2):450–476, AUG 1991. ISSN 0021-9991. doi: 10.1016/0021-9991(91)90285-S.

[23] Marie Farge and Kai Schneider. Coherent vortex simulation (CVS), a semi-deterministic turbulence model using wavelets. Flow, Turbulence and Combustion, 66(4):393–426, 2001.

[24] E. Feireisl, J. Neustupa, and S. Stebel. Convergence of a Brinkman-type penalization for compressible fluid flows. Journal of Differential Equations, 250:596–606, 2011.

[25] Bengt Fornberg. A numerical study of steady viscous flow past a circular cylinder. Journal of Fluid Mechanics, 98:819–855, 1980.

[26] H Foysi, S Sarkar, and R Friedrich. Compressibility effects and turbulence scalings in supersonic channel flow. Journal of Fluid Mechanics, 509:207–216, 2004.

[27] J. B. Freund. Proposed inflow/outflow boundary condition for direct computation of aerodynamic sound. AIAA Journal, 35(4):740–742, 1997.

[28] Massimo Germano, Ugo Piomelli, Parviz Moin, and William H Cabot. A dynamic subgrid-scale eddy viscosity model. Physics of Fluids A: Fluid Dynamics, 3(7):1760–1765, 1991.

[29] Sandip Ghosal, Thomas S Lund, Parviz Moin, and Knut Akselvoll. A dynamic localization model for large-eddy simulation of turbulent flows. Journal of Fluid Mechanics, 286:229–255, 1995.

[30] Daniel E. Goldstein and Oleg V. Vasilyev. Stochastic coherent adaptive large eddy simulation method. Physics of Fluids (1994-present), 16(7):2497–2513, 2004.

[31] Daniel E. Goldstein, Oleg V. Vasilyev, and Nicholas K.-R. Kevlahan. CVS and SCALES simulation of 3-d isotropic turbulence. Journal of Turbulence, (6):N37, 2005.

[32] C. Jause-Labert, F. S. Godeferd, and B. Favier. Numerical validation of the volume penalization method in three-dimensional pseudo-spectral simulations. Computers and Fluids, 67: 41–56, 2012.

[33] B. Kadoch, D. Kolomenskiy, P Angot, and K. Schneider. A volume penalization method for incompressible flows and scalar advection-diffusion with moving obstacles. Journal of Computational Physics, 231(12):4365–4383, 2012.

[34] Upender K Kaul. Three-dimensional elliptic grid generation with fully automatic boundary constraints. Journal of Computational Physics, 229(17):5966–5979, 2010.

[35] N. K. -R. Kevlahan and J. -M. Ghidaglia. Computation of turbulent flow past an array of cylinders using a spectral method with Brinkman penalization. European Journal of Mechanics B Fluids, 20(3):333–350, 2001.

[36] N. K.-R. Kevlahan and O. V. Vasilyev. An adaptive wavelet collocation method for fluid-structure interaction. SIAM Journal on Scientific Computing, 6(26):1894–1915, 2005.

[37] N. K.-R. Kevlahan, T Dubos, and M Aechtner. Adaptive wavelet simulation of global ocean dynamics. Geoscientific Model Development Discussions, 8(7), 2015.

[38] A. N. Kolmogorov. The local structure of turublence in incompressible viscous fluid for very large reynolds numbers. Dokl. Akad. Nauk SSSR, 1941.

[39] Douglas K Lilly. A proposed modification of the germano subgrid-scale closure method. Physics of Fluids A: Fluid Dynamics, 4(3):633–635, 1992.

[40] Mark N. Linnick and Hermann F. Fasel. A high-order immersed interface method for simulating unsteady incompressible flows on irregular domains. Journal of Computational Physics, 204: 157–192, 2005.

[41] Q. Liu and O. V. Vasilyev. Brinkman penalization method for compressible flows in complex geometries. Journal of Computational Physics, 227(2):946–966, 2007.

[42] S Menon and W-W Kim. High reynolds number flow simulations using the localized dynamic subgrid-scale model. In AIAA, Aerospace Sciences Meeting and Exhibit, 34 th, Reno, NV, 1996.

[43] R. Mittal and G. Iaccarino. Immersed boundary methods. Annual Review of Fluid Mechanics, 37:239–261, 2005.

[44] Parviz Moin, K Squires, W Cabot, and Sangsan Lee. A dynamic subgrid-scale model for compressible turbulence and scalar transport. Physics of Fluids A: Fluid Dynamics, 3(11): 2746–2757, 1991.

[45] Y Morinishi, S Tamano, and K Nakabayashi. Direct numerical simulation of compressible turbulent channel flow between adiabatic and isothermal walls. Journal of Fluid Mechanics, 502:273–308, 2004.

[46] A. Nejadmalayeri, O.V. Vasilyev, and A. Vezolainen. Computational complexity of adaptive les with variable fidelity model refinement. In Proceedings of the Ninth International ERCOFTAC Workshop on Direct and Large-Eddy Simulations (DLES9), 2013.

[47] Alireza Nejadmalayeri, Alexei Vezolainen, and Oleg V Vasilyev. Reynolds number scaling of coherent vortex simulation and stochastic coherent adaptive large eddy simulation. Physics of Fluids, 25(11):110823, 2013.

[48] Alireza Nejadmalayeri, Alexei Vezolainen, Giuliano De Stefano, and Oleg V Vasilyev. Fully adaptive turbulence simulations based on lagrangian spatio-temporally varying wavelet thresholding. Journal of Fluid Mechanics, 749:794–817, 2014.

[49] Alireza Nejadmalayeri, Alexei Vezolainen, Eric Brown-Dymkoski, and Oleg V Vasilyev. Parallel adaptive wavelet collocation method for PDEs. Journal of Computational Physics, 298:237–253, 2015.

[50] Christoffer Norberg. Fluctuating lift on a circular cylinder: review and new measurements. Journal of Fluids and Structures, 17(1):57–96, 2003.

[51] Samuel Paolucci, Zachary J Zikoski, and Damrongsak Wirasaet. WAMR: An adaptive wavelet method for the simulation of compressible reacting flow. part i. accuracy and efficiency of algorithm. Journal of Computational Physics, 272:814–841, 2014.

[52] R. Pasquetti, R. Bwemba, and L. Cousin. A pseudo-penalization method for high Reynolds number unsteady flows. Applied Numerical Mathematics, 58:946–954, 2007.

[53] Richard H Pletcher, John C Tannehill, and Dale Anderson. Computational fluid mechanics and heat transfer. CRC Press, 2012.

[54] I. Ramière, P. Angot, and M. Belliard. A fictitious domain approach with spread interface for elliptic problems with general boundary conditions. Comput. Methods Appl. Mech. Engrg., 196:766–781, 2007.

[55] Scott J. Reckinger, Daniel Livescu, and Oleg V. Vasilyev. Comprehensive numerical methodology for direct numerical simulations of compressible rayleigh–taylor instability. Journal of Computational Physics, 2015.

[56] J. D. Regele and O. V. Vasilyev. An adaptive wavelet-collocation method for shock computations. Int. J. Comp. Fluid. Dyn., 23(7):503–518, 2009.

[57] J D Regele, D R Kassoy, and O V Vasilyev. Effects of high activation energies on acoustic timescale detonation initiation. Combustion Theory and Modelling, 16(4):650–678, 2012.

[58] Olivier Roussel and Kai Schneider. Coherent vortex simulation of weakly compressible turbulent mixing layers using adaptive multiresolution methods. Journal of Computational Physics, 229(6):2267–2286, 2010.

[59] Wybe Rozema, Hyun J Bae, Parviz Moin, and Roel Verstappen. Minimum-dissipation models for large-eddy simulation. Physics of Fluids, 27(8):085107, 2015.

[60] Kai Schneider and Oleg V Vasilyev. Wavelet methods in computational fluid dynamics. Annual Review of Fluid Mechanics, 42:473–503, 2010.

[61] Kai Schneider, Marie Farge, Giulio Pellegrino, and Michael M Rogers. Coherent vortex simulation of three-dimensional turbulent mixing layers using orthogonal wavelets. Journal of Fluid Mechanics, 534:39–66, 2005.

[62] W. Sweldens. The lifting scheme: A construction of second generation wavelets. SIAM J. Math. Anal., 29(2):511–546, 1998.

[63] Christopher K. W. Tam and J. C. Hardin. Second computational aeroacoustics (CAA) workshop on benchmark problems. (3352), June 1997.

[64] H.-Z. Tang, Tao Tang, and Pingwen Zhang. An adaptive mesh redistribution method for nonlinear hamilton–jacobi equations in two-and three-dimensions. Journal of Computational Physics, 188(2):543–572, 2003.

[65] Tao Tang. Moving mesh methods for computational fluid dynamics. Contemporary mathematics, 383:141–174, 2005.

[66] P D Thomas and J F Middlecoff. Direct control of the grid point distribution in meshes generated by elliptic equations. AIAA journal, 18(6):652–656, 1980.

[67] Joe F Thompson, Frank C Thames, and C Wayne Mastin. Automatic numerical generation of body-fitted curvilinear coordinate system for field containing any number of arbitrary two-dimensional bodies. Journal of computational physics, 15(3):299–319, 1974.

[68] Joe F Thompson, Frank C Thames, and C Wayne Mastin. TOMCAT– a code for numerical generation of boundary-fitted curvilinear coordinate systems on fields containing any number of arbitrary two-dimensional bodies. Journal of Computational Physics, 24(3):274–302, 1977.

[69] D. J. Tritton. Experiments on the flow past a circular cylinder at low Reynolds numbers. Journal of Fluid Mechanics, 6:547–567, 1959.

[70] O. V. Vasilyev. Solving multi-dimensional evolution problems with localized structures using second generation wavelets. International Journal of Computational Fluid Dynamics, 17:151–168, 2003.

[71] O. V. Vasilyev and N. K. -R. Kevlahan. Hybrid wavelet collocation - Brinkman penalization method for complex geometry flows. Int. J. Numerical Methods in Fluids, 40:531–538, 2002.

[72] O. V. Vasilyev and N. K. -R Kevlahan. An adaptive multilevel wavelet collocation method for elliptic problems. J. Comp. Phys., 206(2):412–431, 2005.

[73] O. V. Vasilyev and S. Paolucci. A dynamically adaptive multilevel wavelet collocation method for solving partial differential equations in a finite domain. Journal of Computational Physics, 125:498–512, 1996.

[74] O. V. Vasilyev, D. A. Yuen, and S. Paolucci. The solution of PDEs using wavelets. Computers in Phys., 11(5):429–435, 1997.

[75] O. V. Vasilyev, G. De Stefano, D. E. Goldstein, and N. K. -R. Kevlahan. Lagrangian dynamic sgs model for stochastic coherent adaptive large eddy simulation. Journal of Turbulence, (9): N11, 2008.

[76] O.V. Vasilyev and C. Bowman. Second generation wavelet collocation method for the solution of partial differential equations. Journal of Computational Physics, 165:660–693, 2000.

[77] R. Verstappen, S. T. Bose, J. Lee, H. Choi, and P. Moin. A dynamic eddy-viscosity model based on the invariants of the rate-of-strain. In Proc. of the Summer Program, pages 183–192. Citeseer, 2010.

[78] Roel Verstappen. When does eddy viscosity damp subfilter scales sufficiently? Journal of Scientific Computing, 49(1):94–110, 2011.

[79] An-Bang Wang, Zdenek Trávníček, and Kai-Chien Chia. On the relationship of effective Reynolds number and strouhal number for the laminar vortex shedding of a heated circular cylinder. Physics of Fluids, 12:1401–1410, 2000.

[80] Alan M Winslow. Numerical solution of the quasilinear poisson equation in a nonuniform triangle mesh. Journal of computational physics, 1(2):149–172, 1966.